UNIVERISTY OF OKLAHOMA

GRADUATE COLLEGE

LOW-COST VIDEO-OCULOGRAPHY SYSTEM FOR EYE TRACKING

A THESIS

SUBMITTED TO THE GRADUATE FACULTY

in partial fulfillment of the requirements for the

Degree of

MASTER OF SCIENCE

By

MATTHEW SMITH
Norman, Oklahoma
2023

LOW-COST VIDEO-OCULOGRAPHY SYSTEM FOR EYE TRACKING

A THESIS APPROVED FOR THE

STEPHENSON SCHOOL OF BIOMEDICAL ENGINEERING

BY THE COMMITTEE CONSISTING OF

Dr. Chenkai Dai, Chair

Dr. Kuang Hua Chang

Dr. David Miller

Acknowledgements

I would like to express my gratitude to everyone who has assisted me in conducting my research and supported me throughout the process of completing my thesis. The completion of this thesis would not have been possible without the help and guidance of my advisor Dr. Chenkai Dai. His expertise, encouragement, and kindness were crucial for the completion of my work. Thank you for welcoming me into your lab and giving me the opportunity to learn and grow as a researcher. I would also like to extend my thanks to Dr. Kuang Hua Chang and Dr. David Miller for agreeing to be members of my committee and for their time and feedback which was instrumental in refining and strengthening my thesis. Lastly, I would like to thank Ethan Soemantri, Brett Peterson, and Adam Goldberg for their contributions which were vital to the development of the eye tracking device.

TABLE OF CONTENTS

ACKNOWLEDGEMENTS IV
LIST OF FIGURES VII
LIST OF TABLES VIII
ABSTRACT IX
CHAPTER 1. OVERVIEW 1
1.1 Introduction 1
1.1.1 History of Eye Tracking 1
1.1.2 Eye and Vestibular System Anatomy 2
1.2 Eye Tracking Techniques 5
1.2.1 Current Eye Tracking Methods 5
1.2.2 Eye Tracking Principles 7
1.3 The Proposed Device 9
CHAPTER 2. DESIGN DETAILS 11
2.1 Prototype I 11
2.1.1 Hardware 11
2.1.2 Software 13
2.2 Prototype II 15
2.2.1 Hardware 16
2.2.2 Software 19
2.2.3 Methods 20
2.3 Final Design 21
2.3.1 Hardware 21
2.3.2 Software 22
CHAPTER 3. RESULTS 29
3.1 Prototype I Results 29
3.2 Prototype II Results 31
3.3 Final Design Results 32
CHAPTER 4. DISCUSSION 35
CHAPTER 5. CONCLUSION 39

CHAPTER 6. OTHER PROJECT 40
6.1 Abstract 40
6.2 Introduction 41
6.3 Methods 42
6.4 Discussion 46
6.5 Results 51
6.6 Conclusion 52
BIBLIOGRAPHY 53
APPENDIX 58

List of Figures

Figure 1.1	Human Eye Anatomy	2
Figure 1.2	Vestibular System Anatomy	3
Figure 1.3	Scleral Search Coil Eye Tracking	5
Figure 2.1	Prototype I	11
Figure 2.2	Object Detection Model Labeling and Output	13
Figure 2.3	Prototype II	15
Figure 2.4	Wiring Diagram for Accelerometer and Gyroscope	17
Figure 2.5	Improved Lighting Conditions	18
Figure 2.6	Improved Lighting Model	19
Figure 2.7	Improved Training Steps Model	20
Figure 2.8	Final Headset Design	21
Figure 2.9	Classification Loss Improvements	23
Figure 2.10	Localization Loss Improvements	24
Figure 2.11	Regularization Loss Changes	26
Figure 2.12	Total Loss Changes	27
Figure 3.1	Prototype I Gyroscope Results	30
Figure 3.2	Prototype I Pupil Center Tracking	30
Figure 3.3	Prototype II Pupil Center and Gyroscope Results	31
Figure 3.4	Final Design Pupil Center and Gyroscope Results	32
Figure 6.1	Experimental Setup	43
Figure 6.2	Scanning Point Removal	44
Figure 6.3	Illustration of Data Preprocessing	45
Figure 6.4	TB Tympanometry Measurements	46
Figure 6.5	Pre and Post Injection Absorbance Averages	47
Figure 6.6	Comparison of Sound Displacements	48
Figure 6.7	TM Quadrant Division	49
Figure 6.8	Surface Variation and Area to Volume Ratio Results	50

List Of Tables

Table 3.1	Final Design Correlation and Average Gain	34
Table 4.1	Price Breakdown of the Device	38

ABSTRACT

The vestibular system plays a critical role in balancing and the vestibulo-ocular reflex (VOR), which aids in maintaining visual stability during head movements. Current methods of vestibular research rely on scleral coils and video-oculography (VOG) with markers. These processes are potentially damaging to the test subject and painful. A comfortable non-invasive procedure is VOG without the use of markers. However, this option foregoes the accuracy of the others. A machine learning approach was explored to see if this gap in functionality could be closed. VOG is a visual-based technique of measuring eye movements. This method is used in vestibular and oculomotor research and medical diagnosis involving vertigo and stroke. A Machine Learning system was developed by training object-detection models from TensorFlow with a headset fabricated for this project. The horizontal/vertical movements were tracked by recording the model's bounding box. From the bounding box, the center of the pupil can be derived via the geometric center. The location of the pupil center is used to calculate the angular velocity of the eye. A 3d-printed headset was fabricated to test the system using a gyroscope, raspberry pi, button light, and camera. The headset's rotational data collection is processed along with the images captured. The rate of error was calculated to be more than scleral coils, although a more thoroughly trained model could be able to reduce error. The pupil miss rate limits the accuracy but using a higher speed and resolution camera will ameliorate the problem. A machine learning process was explored for the use of vestibular-ocular research in 2D. A low-cost headset was fabricated as an alternative to the current methods which are significantly more expensive.

Chapter 1. Overview

1.1 Introduction

1.1.1 History of Eye Tracking

Eye tracking technology, despite being considered a modern invention, has been utilized since the late 1800s when psychologist Louis Emile Javal began researching eye movement during reading [1]. In the early 1900s psychologist Alfred Yarbus utilized the corneal reflection technique to study eye movements and visual perception. This technique bounced light off the cornea of the eye and recorded the reflection to track the movements of the eye with a high degree of accuracy [1,2]. The development of computer technology and software in the 1990s, along with digital cameras becoming affordable, led to the creation of more advanced eye-tracking systems capable of recording eye movements with greater precision. These systems have been used in fields such as human-computer interaction, assistive technology, and are increasingly employed as a tool to diagnose and monitor neurological disorders [3-6].

Neurological disorders can impact eye movement and eye tracking technology can detect and analyze these changes For example, gaze estimation aids in diagnosing autism and attention deficit hyperactivity disorder (ADHD) as children with autism struggle with making and sustaining eye contact while children with ADHD have difficulty sustaining attention/gaze [7-9]. Our research aims to create a diagnostic tool for a wide range of neurological disorders including stroke, multiple sclerosis, early onset ataxia, concussion, and vertigo by tracking eye movement, gain, and the vestibulo-ocular reflex (VOR).

1.1.2 Eye and Vestibular System Anatomy

The vestibular system plays a crucial role in maintaining balance and equilibrium. The vestibulo-ocular reflex (VOR) assists in stabilizing visual gaze during head movements. To track the VOR, a machine learning-based video-oculography (VOG) device without markers was developed. VOG is a widely used visual-based process for measuring eye movements. Before discussing the intricacies of our VOG system without markers, a brief introduction to the anatomy of the eye and the vestibular system is necessary.

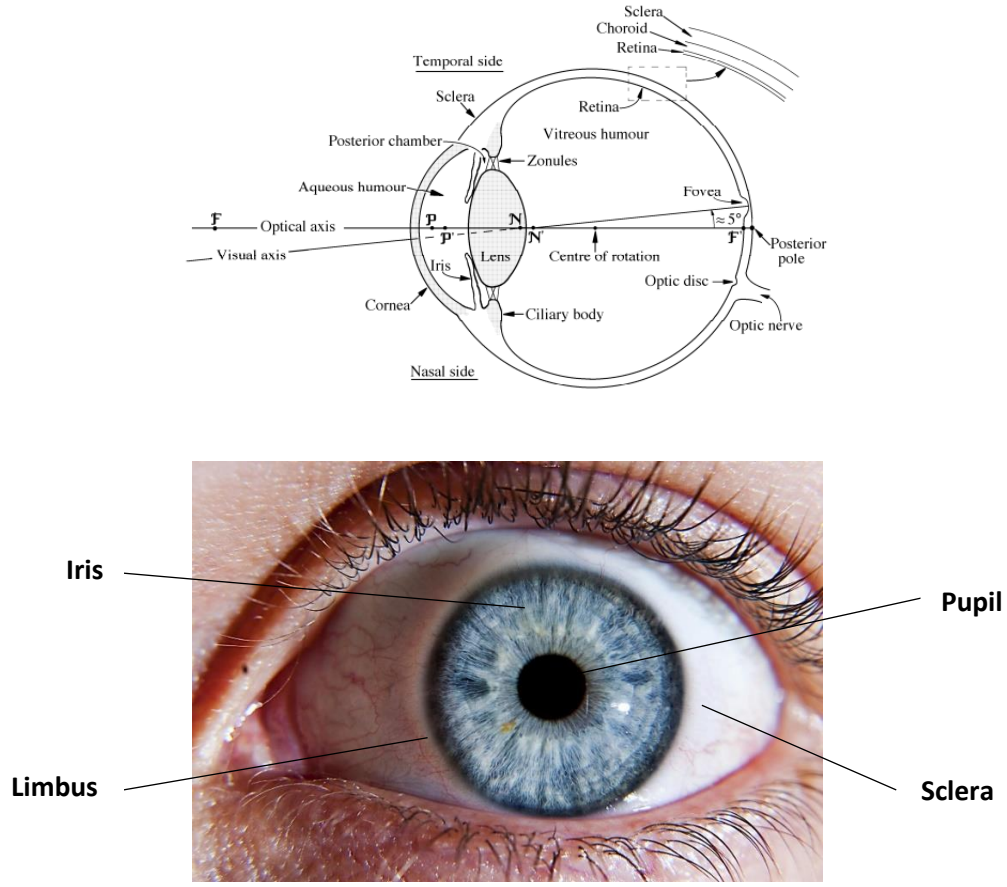

Figure 1.1 Human Eye Anatomy (a) Sagittal illustration of the anatomy of the human eye [10] (b) Coronal view of the human eye with iris, pupil, limbus, and sclera labeled [11].

Figure 1.1 shows the anatomy of the human eye. The cornea is the front of the eye and is a transparent layer that protects the eye from outside damage. Behind the cornea is the iris which is the colored part of the eye. The iris controls the size of the pupil which in turn controls the amount

of light let in. Between the iris and the cornea is a layer of aqueous humor that enables the passage of light, provides nutrients, and aids in maintaining intraocular pressure. The pupil is located inside the iris and helps focus the light which is then passed to the retina. The retina receives this focused light and converts it into neural signals that are sent through the optic nerve to the brain. The retina transforms the light signal into electrical signals through its cone and rod cells. The cone cells allow the eye to make out fine details and colors. The rods allow for less focused vision but can better track movements and mostly make up the peripheral view. Directly behind the pupil is the posterior pole and just above it is the fovea. The fovea is a small pit in the retina that is made up of exclusives cone cells. A line drawn from the fovea to the center of the pupil is the visual axis. The visual axis is where our eye is focusing at any given time and is much clearer than peripheral vision. The brain then decodes the electrical signals which result in vision.

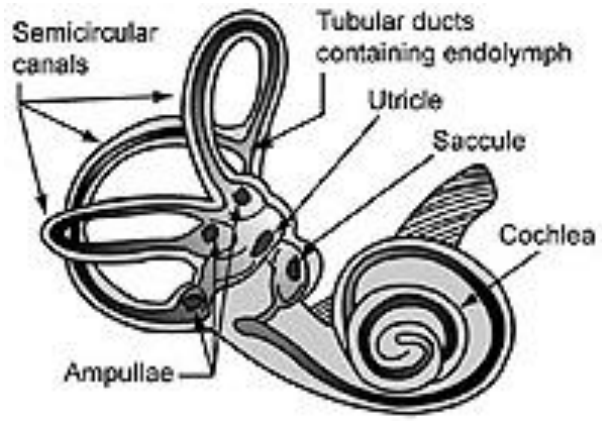

Figure 1.2 Vestibular System Anatomy. Illustration of the anatomy of the inner ear with the semicircular canals, utricle, and saccule labeled [12].

The vestibular system consists of three semi-circular canals that detect angular acceleration and the utricle and saccule which detect linear acceleration, gravitational acceleration, and position of the head [13]. The utricle is a small, fluid-filled sac located in the inner ear. It is one of the two otolith organs. Within the utricle are hair cells, called stereocilia, that are covered with tiny calcium

carbonate crystals called otoliths. When the head movement occurs, the otoliths move along with the fluid in the utricle, which causes the stereocilia to bend. This bending generates electrical signals that are sent to the brain via the vestibular nerve. The brain uses these signals to determine the orientation of the head and the direction and speed of movement in order to help maintain balance and stabilize the eyes during head movements [14]. The saccule is the other otolith organ located in the inner ear and is located adjacent to the utricle. The saccule works almost identically to how the utricle does. However, the saccule is oriented vertically, whereas the utricle is oriented horizontally. This means the saccule is responsible for detecting vertical linear acceleration, while the utricle is responsible for detecting horizontal linear acceleration. The three semi-circular canals are the other major components of the vestibular system and are fluid-filled tubes that are oriented perpendicular to each other. Each semi-circular canal is responsible for sensing rotational acceleration for one of the three dimensions. The semi-circular canals have a wider region called the ampulla, which contains stereocilia that are embedded in a gelatinous structure called the cupula. When the head rotates in a particular direction, the fluid in the corresponding semicircular canal moves, causing the stereocilia to bend the cupula creating a signal. As the head rotates, the generated electrical signals are transmitted to the brain via the vestibular nerve. The brain uses these signals to determine the direction, speed, and duration of the head movement [14]. The semicircular canals work in combination with the utricle and saccule to provide a comprehensive picture of the body's position and movement. The vestibular system's purpose is to maintain balance, stabilize vision, and coordinate movements. VOG will be used to track an individual's VOR to gain insight into neurological conditions. The VOR is the three semi-circular canals working with the utricle and saccule in order to send excitatory signals to the oculomotor nuclei for the opposite direction of acceleration detected and inhibitory signals to the oculomotor neurons

for the same direction [13]. These signals cause saccadic eye movement in the opposite direction of the acceleration detected by the stereocilia which allows for the gaze to remain steady while the head is moving.

1.2 Eye Tracking Techniques

1.2.1 Current Eye Tracking Methods

The current methodologies used for tracking the VOR's response include scleral search coils or electro-oculography (EOG), infrared-oculography (IRO), and VOG. Scleral search coil eye tracking is widely regarded as the gold standard for eye tracking and is often implemented in animal studies due to its high accuracy [15]. This method utilizes a small magnetic coil implanted on the sclera which generates a small electrical current induced by the magnetic field within the coil, that is tracked to determine the movement of the eye [16]. However, the invasive and painful nature of this method makes it impractical for use in human subjects.

(a)  (b) 

Figure 1.3 Scleral Search Coil Eye Tracking. (a) Scleral search coil made of silicone rubber annulus with induction coils of insulated copper wire inserted into the silicone contact [17]. (b) Image of the scleral search coil attached to the eye [18].

There are two different methods of VOG used in eye tracking. The first method is VOG with markers. This method uses small reflective markers placed on the surface of the eye, which

are tracked throughout the video recording to determine eye movement. This method yields a high level of precision that is comparable to EOG [19]. However, the markers can be uncomfortable for some participants, and may shift during the experiment and cause inaccurate results. Additionally, the use of reflective markers can interfere with the participant's vision, which may affect their ability to complete visual tasks. Despite these limitations, VOG with markers is a less painful procedure than EOG which makes it slightly more practical for use in humans, yet, it is still mostly used exclusively in animal research [19]. The other method is VOG without markers. This method uses cameras to record the eye's response to visual stimuli. This method is less accurate than VOG with markers but is less invasive. It also has significantly more difficulty tracking eye torsion than its marker counterpart. The two methods for eye tracking with VOG without markers are corneal reflection and pupil center tracking. Corneal reflection VOG tracks the reflection of a light source, either visible light or infrared, on the cornea as the eye moves. The position of the corneal reflection is used to calculate the direction and amplitude of eye movements. The main advantage of corneal reflection VOG is its high spatial resolution, which allows for highly accurate measurements of eye movement. Corneal reflection also allows for more precise torsional tracking. However, this technique is susceptible to artifacts from head movement or blinking, which can distort and lead to inaccuracies. Pupil center tracking VOG, on the other hand, tracks the movement of the pupil center as the eye moves. This method is less susceptible to artifacts from head movement as the pupil is relatively stable during these movements. Pupil center tracking VOG has lower spatial resolution compared to corneal reflection VOG, but it is more reliable in measuring slow eye movements and detecting subtle changes in eye position [20]. When compared to scleral search coil tracking, VOG costs less and is non-invasive making it an ideal tool for human studies. However, it is more prone to errors, often caused by blinking or lighting environment, than EOG.

IRO utilizes similar methods as VOG, however, instead of visible light, it uses infrared light and instead of a camera an IR detector can be used. IRO can track both corneal reflection and pupil center. IRO using corneal reflection tracks the infrared light that is reflected off the cornea instead of the pupil or another feature. IRO using pupil center tracking is less biases towards colored eyes than its VOG counterpart. IRO is less affected by lighting environments leading to a more accurate measurement than VOG.

1.2.2 Eye Tracking Principles

VOG with markers utilizes a feature-based algorithm, while VOG without markers can use feature based or model-based algorithms. Feature based algorithms rely on detecting specific features of the eye, such as edges, corners, or a marker. Those features are then used to estimate the position of the gaze. These algorithms often require careful calibration, and the experiment must be set up to account for variations in lighting, head movement, and other factors that can affect the features being tracked such as eye lashes blocking the feature. Common feature-based algorithms include corneal reflection, pupil center tracking, and VOG with markers. Model-based algorithms, on the other hand, use a mathematical model of the eye to predict the position of the gaze. For example, an object detection model can be used to find the best fitting ellipse for the pupil [21, 22]. Feature-based algorithms are usually simpler and faster to implement but are more sensitive to environmental factors such as light. Model-based algorithms are more robust but often require more computational resources and expertise to develop.

Most eye tracking systems are either head-mounted or remote systems. A remote eye tracking system is a type of technology that allows for tracking and analyzing eye movements and gaze patterns from a distance. Remote video-based eye tracking systems can utilize both infrared and visible spectrum tracking. One of the main advantages remote systems have overhead mounted

systems is that they capture head movement that is not affected by any external factors such as the weight a head mounted system would entail. However, these systems require the user to be in a specific area of operation. Remote eye tracking systems are also usually considerably less accurate than their head mounted counterparts. Because of the low accuracy and limited area of operation, remote eye tracking systems are not usually used in clinical settings. They are more often used in research and commercial settings where users are interacting with a website or application to track generally where the user is looking. This technology can help impaired individuals operate computers. These systems are simple and provide accurate enough gaze estimation for commercial settings, yet they lack the level of accuracy desired to aid in clinical diagnosis. Head mounted systems on the other hand provide adequate accuracy for clinical settings. A head-mounted eye tracking system uses sensors mounted on a headset or glasses to track eye movements and gaze patterns in real-time. The system typically consists of a lightweight and portable headset or glasses that are equipped with cameras that capture eye movement data. The sensors used in head-mounted eye tracking systems typically track the position of the eyes and the movement of the pupils, allowing researchers to measure a wide range of eye movement parameters, including fixation duration, saccade velocity, and smooth pursuit tracking. While head mounted eye tracking systems require more complex equipment and software than remote eye tracking systems, this tradeoff is acceptable because of the significant increase in accuracy and area of operation.

There are two ways to illuminate the eye for tracking, dark and light pupil tracking. In light pupil tracking, the light is placed near the optical axis and causes the pupil to appear brighter than the surrounding iris which is what causes red eyes in photos. The simplicity of bright pupil tracking comes at a price. The main drawbacks are that the size of the pupil, age, ethnicity, and light in the surrounding environment can cause variance in the accuracy of pupil tracking [23]. The other

major drawback was that the camera is set up on the optical axis, which made it near impossible to have the light in the optical axis without mirrors. Due to these limitations, dark pupil tracking was chosen instead. Dark pupil tracking has the light off the optical axis and causes the pupil to appear darker than the surrounding iris. Dark pupil tracking also appeared more accurate for all ethnicities compared to bright pupil tracking which has significant accuracy drops with small dark eyes.

1.3 The Proposed Device

The goal of this project is to combine several of the eye tracking methodologies currently used to create a product that has accuracy comparable to EOG while remaining non-invasive and inexpensive. The basis of our device will be a VOG without markers head mounted device because of the low cost and complexity. It will utilize a model-based algorithm in the form of a machine learning object detection model that will be trained to find the pupil in an image. This machine learning model-based approach should help to maximize accuracy while not adding cost. However, it will be more computationally taxing. Our device will also utilize infrared lighting to reduce the effect of lighting environment and head movement. Along with the added benefit of highlighting the contours of the pupil and limbus and being less biased than bright pupil tracking. This device will be able to track both eye movement and head rotation to compute the gain or ratio between eye and head rotation. By finding an individual's gain, we hope to aid in the diagnosis of stroke, multiple sclerosis, early onset ataxia, concussion, and vertigo. Vertigo is the sensation of spinning or dizziness caused by head movement or visual stimulation. VOG can also help differentiate between peripheral and central causes of vertigo. Peripheral vertigo is caused by disorders of the inner ear, while central vertigo is caused by dysfunction in the brainstem or cerebellum [24]. By analyzing the patterns of eye movements, VOG can help identify the type of problem and

differentiate between these two types of vertigo [25]. Dizziness and imbalance are common symptoms of patients seeking attention in emergency departments; however, these symptoms can stem from both vertigo and stroke. Stroke can cause damage to the brainstem or cerebellum which in turn can cause nystagmus, or “dancing eyes”, which is involuntary eye movement that can be tracked with VOG [26-28]. It is important to be able to distinguish vestibular diseases from stroke in emergency situations as most pharmacological stroke treatments to break up the clot must be given within five hours of the onset of symptoms. VOG has been shown to be capable of differentiating between the two with a series of tests called HINTS, or head impulse test, nystagmus, and test of skew [26, 29, 30]. This device can also aid in Multiple Sclerosis diagnosis. Multiple sclerosis is a neurological disorder that affects the central nervous system. More specifically it is the breakdown of the myelin sheath that surrounds the axon of a neuron whose role is to accelerate the propagation of the action potential. Multiple sclerosis affects the transport of information from one neuron to another and can cause nystagmus or slowed eye movement. This device will help detect subtle changes in eye movement not visible to the naked eye which can help identify early signs of multiple sclerosis [31, 32]. It can also be helpful in monitoring the progression of the disease. VOG can also aid in the diagnosis of early onset ataxia, which is characterized by a lack of muscle control during voluntary movements, and can help distinguish between inherited chronic ataxias and Friedreich ataxia [33]. VOG is also capable of monitoring and assessing the severity of a concussion [34]. In addition to diagnosis, VOG can also be used to monitor the progress of treatment and assess the effectiveness of therapies such as vestibular rehabilitation exercises. However, VOG should not be used as the sole diagnostic tool but should be used in combination with other diagnostic tools for improved diagnostic accuracies.

Chapter 2. Design Details

2.1 Prototype I

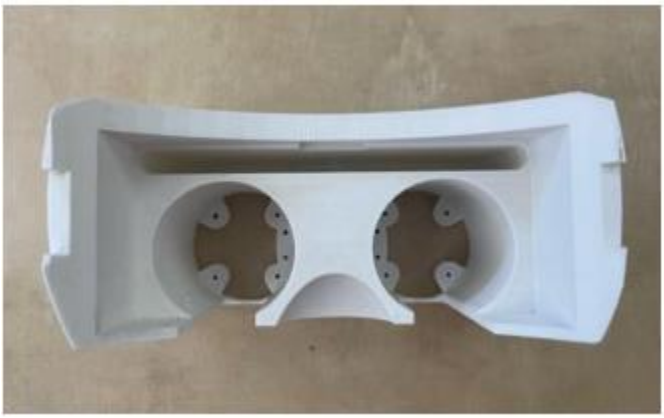

Figure 2.1 Prototype I. Prototype of the 3D printed video-oculography headset without the cameras, Raspberry Pi, and smartphone attached. The two eye holes are intended for the cameras, the top hole is for the smartphone, and the Raspberry Pi will be secured on top. The strap mounts are located on the side and are broken.

2.1.1 Hardware

To develop the initial prototype of the video-oculography headset, a 3D model was constructed in SolidWorks. The design consists of two camera slots, a slot for a smartphone, a nose notch, a Raspberry Pi mounting spot, and two strap mounts. The decision to employ straps for securing the headset to the head was based on the convenience of adjusting the length to accommodate various head sizes. The placement of the two strap mounts was strategically selected to prioritize stability, thereby capturing precise pupil responses without any interference from the device shifting on the head. Holes for the Raspberry Pi Camera and lens are designed to be pressed fit into the sockets. Space for the Raspberry Pi was allotted on the top of the headset for ease of alteration. A Raspberry Pi 4 Model B was chosen because it is compact and light weight which allowed for it to be mounted on top of the headset. The Raspberry Pi 4 is a small single-board

computer that is incredibly versatile while remaining affordable. The quad-core ARM Cortex-A72 processor with 8GB of RAM is powerful enough to support all the software. The software is open source which made control and integration of the cameras and IMU easier through the ability to modify source code. The Raspberry Pi can also interface with a variety of devices. All these factors together make the Raspberry Pi an ideal device for prototyping. Two 12.3 MP Raspberry Pi HQ Camera CS with Arducam 2.8-12 mm Varifocal C-mount lenses attached were chosen because of their compatibility with the Raspberry Pi, high quality footage, and affordable price. The camera's compact design along with high quality video via a 12-megapizel Sony IMX477 sensor made it the ideal camera for our design. The lenses help to improve the resolution of the video and have an adjustable focal length which yields flexibility in the depth of the captured video. However, these benefits are mitigated by the bulk of the lenses which make the device considerably heavier. The cameras were connected to the Raspberry Pi with the Multi Camera adapter Module V2.2 for Raspberry Pi. The headset was 3D printed using PLA+. PLA+ was chosen for the material because of its smooth surface, which reduces friction against the head, glossy/reflective finish, which is utilized to reflect the small light button to increase the exposure of the eye, and affordable price. Small LEDs were attached to the inner side wall of the headset.

2.1.2 Software

A) 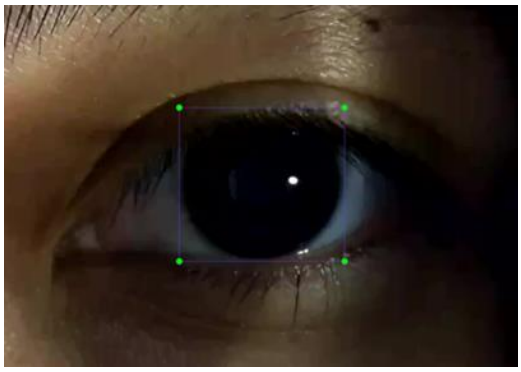 B) 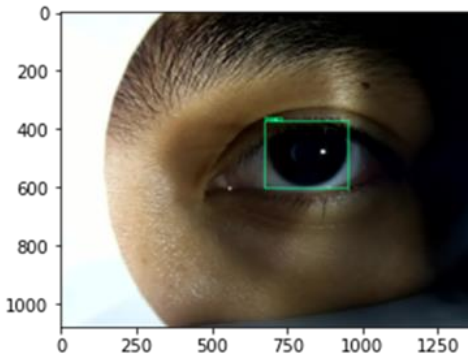

Figure 2.2 Object Detection Model Labeling and Output A) A sample of one of the 300 annotated images used to train the objection-detection model made with the program labelImg. The annotation consists of dragging the bounding box until it encompasses the pupil. B) The output of the trained model is shown with a bounding box encompassing the pupil.

To create a machine learning object detection model, TensorFlow, an open-source software library developed by Google, was utilized. TensorFlow operates on a computational graph that represents a mathematical model as interconnected nodes where each node represents a mathematical operation, and the edges depict the data flow between them. The Python API was employed to define and manipulate these computational graphs. The decision to use TensorFlow was based on its open-source nature, enabling the use of pre-trained models and access to tutorials and code sources, which simplified the coding process while being completely free.

An object detection model is a computer vision task involving identifying and localizing a feature in images or videos. The object detection model uses a convolutional neural network (CNN), which is a deep learning architecture that can learn to identify features in images. CNNs are typically trained using a loss function, such as the mean squared error or cross-entropy loss. The choice of architecture varies depending on its intended use. The main trade-off is between speed and accuracy. In this case, accuracy was prioritized over speed because of the post-processing approach employed.

To train the object detection model a dataset of images with the location and type of feature labeled are necessary. Three-hundred images were acquired by taking an initial nine pictures of the eye with the pupil in each of the following positions: center, up, down, left, right, upper-left, upper-right, lower-left, and lower-right. Then eleven additional images were captured in positions between the initial nine. This was done to provide the objection-detection model with adequate data to train on. Before training the model, the images must be preprocessed by normalizing pixel values and ensuring the images are the same size. The 300 images included multiple people of different ethnicities with different colored eyes. Training on diverse training data is an important consideration to avoid a biased model. The training data must be representative of the real-world scenario where the model will be used. The model is intended for medical diagnosis meaning any individual could be tested. This is why we regularly reevaluated the performance of the model on a diverse group of individuals. The images were then annotated to provide the necessary feature label. To annotate the images, *LabelImg* software was utilized to create bounding boxes centered on the pupil. Another important consideration for maximizing the accuracy of the model is to ensure that each of the labeled images is accurate and consistent. To avoid inconsistencies, the same individual labeled each image and had the bounding boxes edges line up with the top/bottom and right/left of the limbus.

Once the model is trained, it is necessary for it to be evaluated on a separate validation set to measure its performance on unseen data. Common metrics for object detection include precision, recall, and mean average precision (mAP). Precision measures the proportion of predicted object detections that are correct, while recall measures the proportion of true object detections that are detected. mAP is a summary metric that combines both precision and recall across a range of detection thresholds. If the model performance is unsatisfactory, it may be

necessary to adjust the model architecture, hyperparameters, or data preprocessing steps and retrain the model. Hyperparameters that can be tuned include learning rate, batch size, and regularization strength.

A machine learning system was developed by training an object-detection model from using 300 annotated images of the eye. The 300 images included multiple people with different colored eyes After the images were labeled, the object-detection model was trained to an output of a bounding box around the pupil. This allowed us to begin tracking the eye's movement. Eye movements can be broken down into two parts: horizontal/vertical and torsional. In our preliminary approach the horizontal/vertical movements were measured using the model's bounding box. The center of the pupil was derived from the geometric center of the bounding box.

2.2 Prototype II

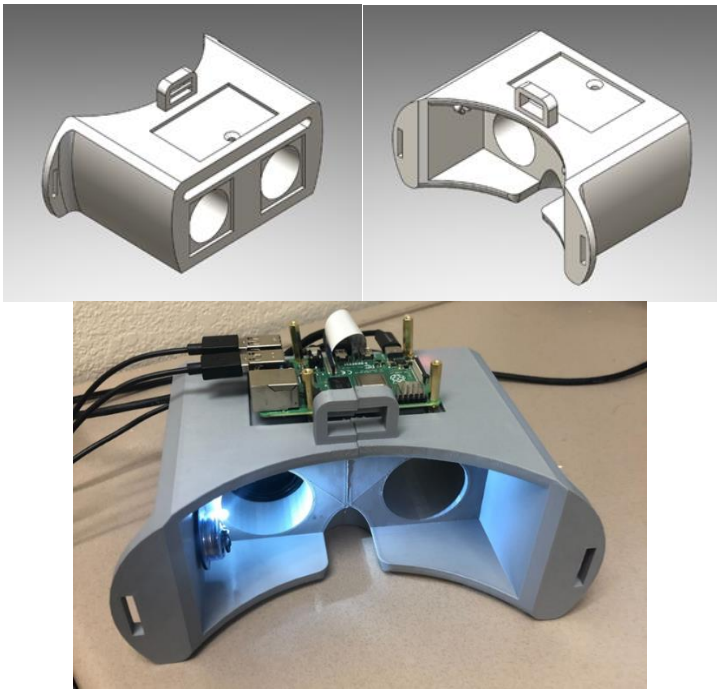

Figure 2.3 Prototype II (a) 3D model of the video-oculography headset made in Solidworks 2021. (b) Prototype of the 3D printed video-oculography headset with the Raspberry Pi attached.

2.2.1 Hardware

Following the preliminary approach, several areas for improvement were identified. Firstly, the strap mount was found to be insufficient in supporting the weight of the device, as illustrated in Figure 2.1. Consequently, a third strap mount was added to enhance the device's strength and stability, and the mounts were repositioned farther from the head to facilitate easier attachment of the straps. Secondly, the nose notch was found to be sharp and too close to the face, resulting in discomfort and device shifting during testing. To address this issue, the notch was relocated further from the head, allowing for a pocket to be created to accommodate the nose, ensuring a pain-free procedure and accurate results. Finally, the use of battery-powered light buttons was adopted instead of a wired connection to improve cable management, reduce the risk of electrical hazards, and provide more space for other devices to be attached to the Raspberry Pi. This modification also facilitated troubleshooting by simplifying the identification of disconnected wires.

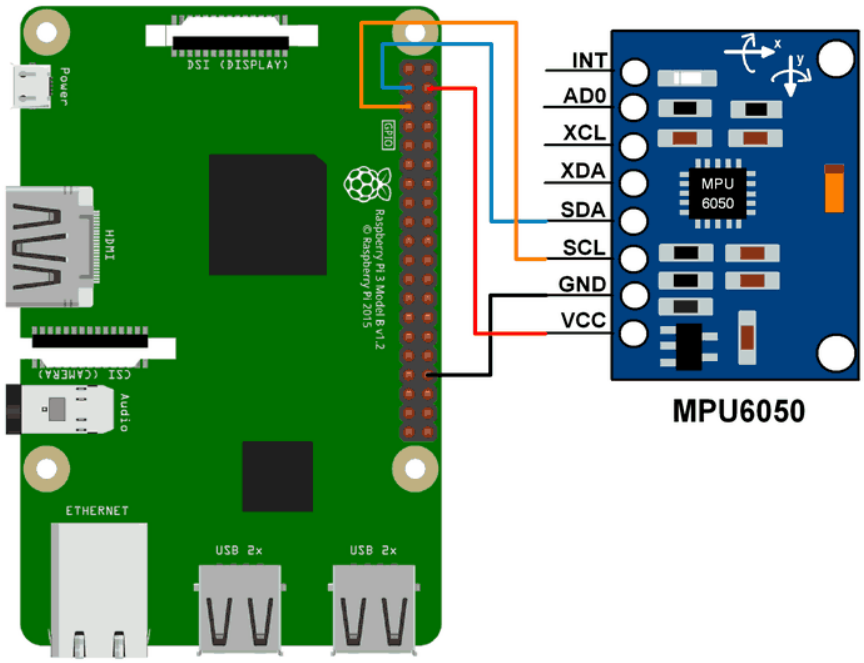

Figure 2.4 Wire Diagram for Gyroscope and Accelerometer. The complete wiring diagram for the Raspberry Pi can be found in the appendix. The gyroscope and accelerometer are powered with 5V.

The next improvement would be utilizing an accelerometer and gyroscope instead of the Phyphox iPhone application. The headset's gyroscopic and accelerometer data collection was compounded to create an inertial measurement unit (IMU). An IMU utilizes the specific force or acceleration from the accelerometer and the angular rate or velocity from the gyroscope in order to estimate the motion, orientation, and position of the device in three dimensions. The accelerometer measures the acceleration of the device in three axes of motion, up/down, forward/back, and up/down, while the gyroscope measures the rotation around each of the axes. The gyroscope is best utilized for quick or sharp movements; however, the main disadvantage is that over time the gyroscopic data drifts and begins to diverge from accurate results. An accelerometer is poor at measuring short quick changes; however, it is accurate over time. To provide the most accurate data over time from the accelerometer and gyroscope a complementary filter was utilized. The complementary filter fuses the high frequency data measured by the

gyroscope and the low frequency data measured by the accelerometer to estimate the movement, orientation, and position of the device. The complementary filter places most of the weight in the gyroscopes data because it estimates the orientation of the device and is more accurate in the short term but utilizes the accelerometers data to prevent the data from drifting over time. This filter utilizes the strengths of both of the sensors while minimizing their weaknesses. The raw IMU data collected is filtered prior to being input into the complementary filter to reduce noise. The gyroscopic data is prone to low frequency noise, so it is passed through a high pass filter, while the accelerometer data is prone to high frequency noise, so it is passed through a lowpass filter.

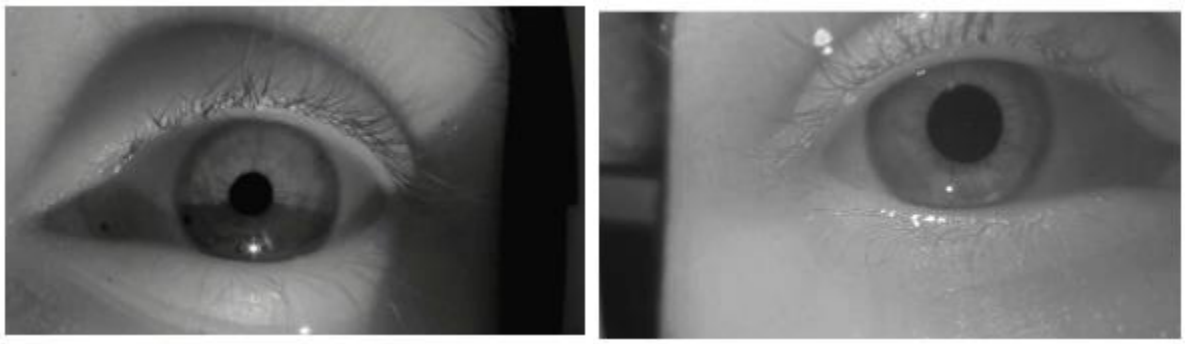

Figure 2.5 Improved Lighting Conditions. (a) Image captured by prototype I with only one light source. (b) Image captured by prototype II with two light sources

Another improvement implemented in the second prototype was the modification of the lighting conditions. In the initial design, a single light source was positioned on the bottom left side of the headset. However, this configuration presented several issues, such as shadows, reflections, and an unbalanced lighting environment. In particular, the single light source produced a noticeable shadow on the lower part of the eye, as illustrated in figure 2.5. These shadows could potentially interfere with the accuracy of eye tracking and alter the intensity gradient. To overcome this challenge, a second light source was integrated into the headset, located on the top of the device. This resulted in a more uniform illumination environment with fewer shadows. The enhancement can be observed by comparing Figure 2.5a with 2.5b.

2.2.2 Software

The first improvement was to train the model based on the improved lighting conditions of less shadows and better balance caused by adding a second light.

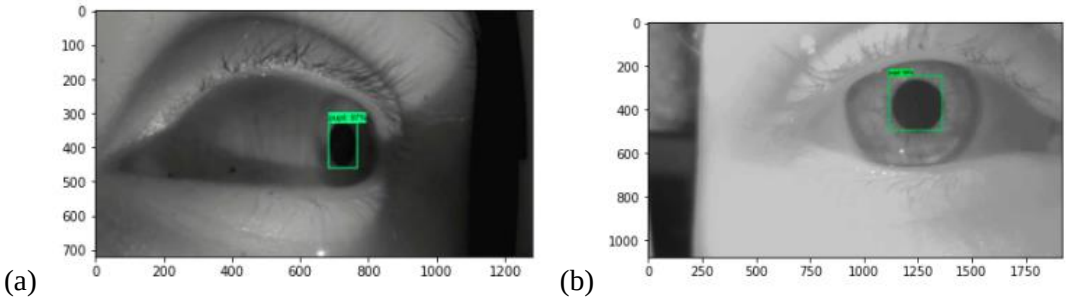

Figure 2.6 Improved Lighting Model. (a) Old detection model trained on singular light source images with shadows and low brightness with a training rate of approxiamtely 97%. (b) Improved detection model trained on two light sources with improved brightness with a training rate of approxiamtely 99%.

Figure 2.6 shows the old detection model which was trained using images taken with only one light source and the new detection model which was trained using images taken with two light sources. The reduction of shadows and more even lighting conditions improved the accuracies of images from around 97% with the old model to 99% with the new model. The next improvement made to the object detection model was to increase the number of images the model is trained on from 300 images to approximately 1800 images. The next improvement was to increase the amount of training steps from 3000 to 5000.

(a) 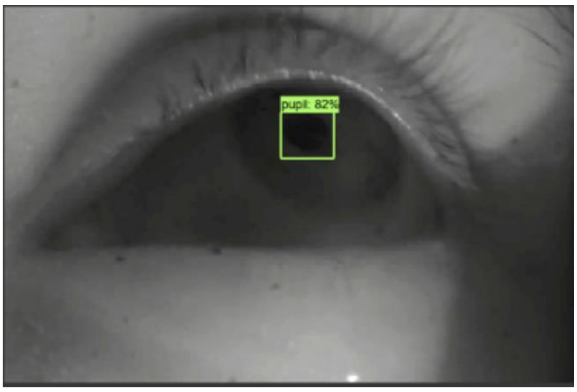

(b) 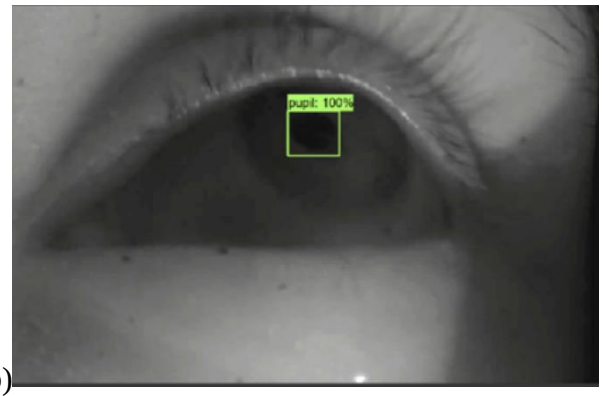

Figure 2.7 Improved Training Steps Model. (a) Detection accuracy of 82% from the detection model with 3000 steps. (b) Detection accuracy of 100% from the detection model with 5000 steps.

Increasing the number of images, the model is trained on allows for better performance as the model is better able to discern between the variations in the data. It also decreases the likelihood of the model overfitting, which is when the model learns patterns from the training data that is not representative of the entire data set. It also increases the model's robustness as it is trained on a more diverse data set. Increasing the training steps can help the model to reach convergence. It also reduces the likelihood of model underfitting, which occurs when the model cannot comprehend the complexity of the data which leads to poor performance. These improvements significantly increased the overall accuracy of the model.

2.2.3 Methods

Workflow:

1. Turn on the Raspberry Pi

2. Open test camera program to ensure the eye is centered and in focus

3. Change the save file name in both the gyroscope and camera programs

4. Open the terminal and run the following command "python3 officialGyro.py & python3 officialCamera.py"

5. Wait until the video shows up on the screen then instruct the subject to turn their head left and right at a rate of 1 hertz. Press ctr + c to end the program.

6. Transfer the data from the raspberry Pi to a desktop either by emailing or with a thumb drive.

7. Open the video manipulation program to separate the video into frames.

8. Open the training and detection program in google colab in order to gain the pupil center positional data.

9. Upload the positional data into the MATLAB program to calculate gain

2.3 Final Design

2.3.1 Hardware

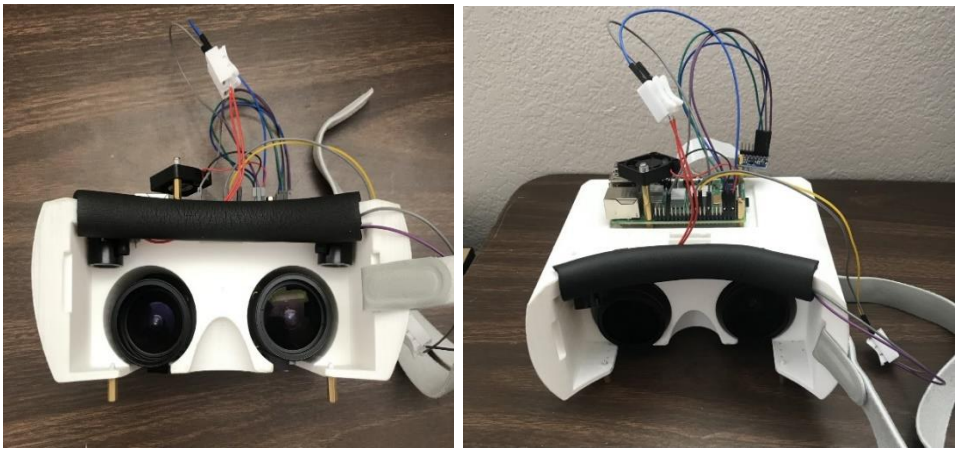

Fig 2.8 Final Headset Design. Final Design of the 3D printed video-oculography headset with the Raspberry Pi, camera, IR light, and fan attached.

The final design of the device involved significant improvements over the preceding versions. In order to increase strength and stability, the strap mounts were altered to resemble the initial prototype, with the holes shifted away from the edge of the device. To reduce weight and

material usage, the mounts were brought back towards the device. The third strap mount, which did not significantly contribute to stability, was removed. A fan was also added to the Raspberry Pi to prevent the central processing unit (CPU) from overheating during demanding computational processes. Overheating can lead to performance issues or even damage the device, and the fan helps increase system stability. Furthermore, to increase user comfort, a soft cushion was added to the part of the device that makes contact with the forehead.

Another improvement was to utilized infrared light. While prolonged exposure to high intensity infrared light can be damaging to the eye, the IR lights used are not powerful enough to cause damage in the short time the eye is tested. The implementation of dark pupil tracking in conjunction with infrared lighting resulted in a more distinct contrast between the iris and pupil. Using infrared lighting allowed for better control over environmental light. The number of lights was kept at two to ensure proper illuminated the eye while reducing the number of shadows in the image. The reduction in shadows allowed for an increase in the accuracy/precision of the device. It also fixed the issue of shadows creating intensity differences. With an evenly lit eye, the striations became visible and trackable.

The last improvement incorporated into the hardware of the device involves utilizing a singular camera, resulting in a significant reduction in cost, as the camera and lens were the most expensive components. This optimization was achievable by enabling the camera to alternate between the two available camera slots, enabling it to capture measurements of both the left and right eye. Additionally, this alteration contributed to a reduction in the overall weight of the device.

2.3.2 Software

In machine learning, loss measures how well a machine learning model is performing on the task it is supposed to accomplish. The goal is to minimize this loss function during training in order to improve accuracy and predictive power. The loss metrics are the most important indicator of training accuracy and overall performance.

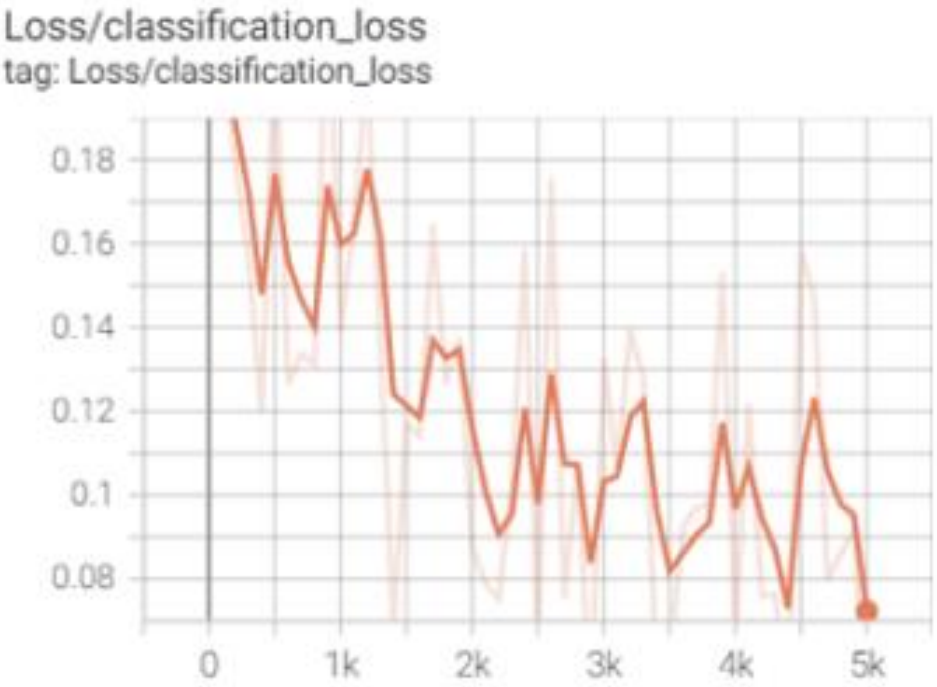

(a)

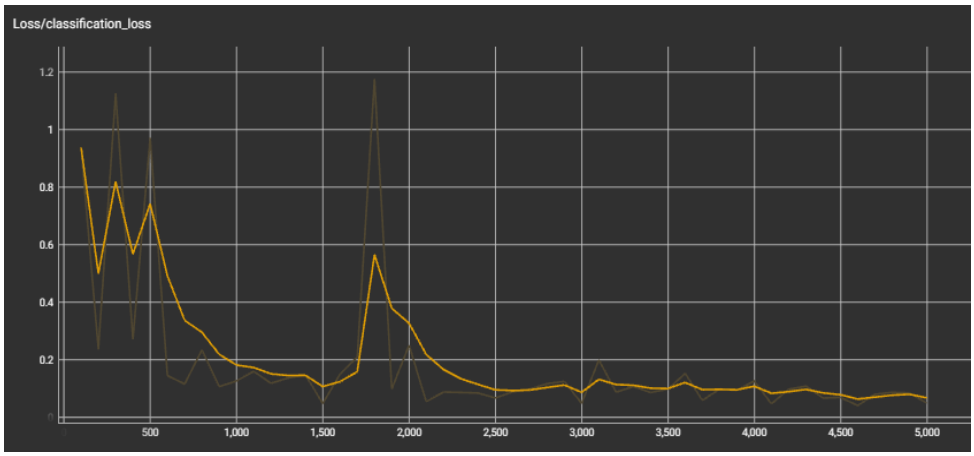

(b)

Figure 2.9 Classification Loss Improvements. (a) Classification loss of the second prototype's object detection model. The raw data is represented by the faded line and the smoothed data is represented by the bright line. (b) Classification loss of the final design's object detection model. The raw data is represented by the faded line and the smoothed data is represented by the bright line.

The first loss metric that will be discussed is classification loss. Classification loss is a specific type of loss function that measures the difference between the predicted class probabilities and the true class labels of a set of training data. Cross-entropy loss is the most common type and is usually used in binary classification and multi-class classification problems. The eye tracking model only has one class, the pupil class, so we utilize binary classification. Cross-entropy loss measures the difference between the predicted probabilities and the true labels by calculating the log loss between the predicted probability distribution and the true label distribution. The better the model is performing on the classification task, the lower the cross-entropy loss will be. Figure 2.9 shows the improvement of the classification loss between the old and new object detection model.

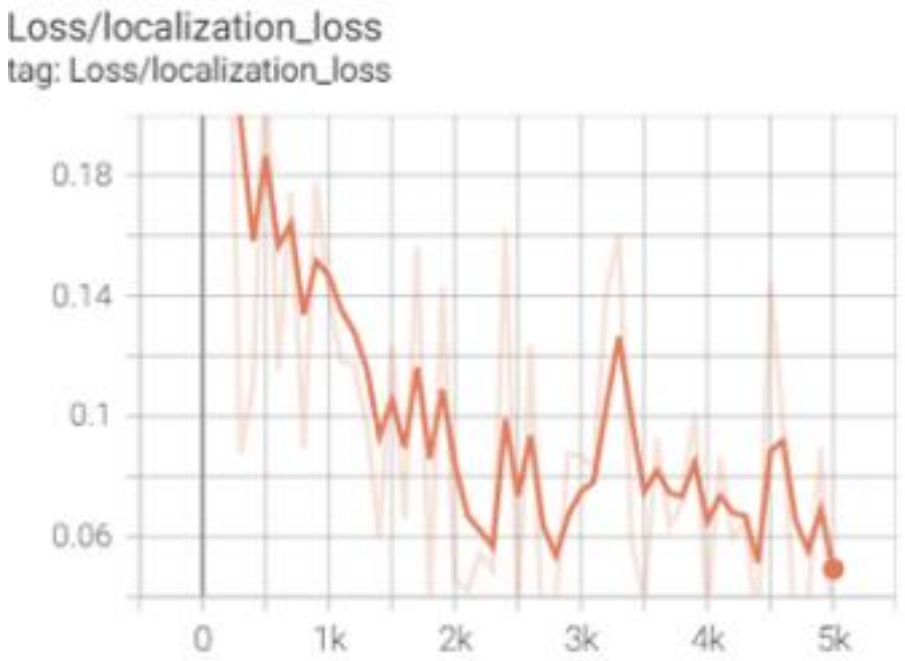

(a)

(b) 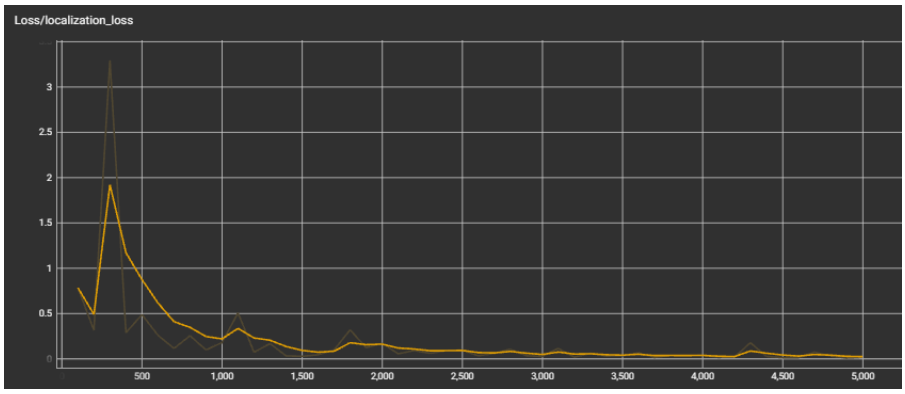

Figure 2.10 Localization Loss Improvements. (a) Localization loss of the second prototype's object detection model. The raw data is represented by the faded line and the smoothed data is represented by the bright line. (b) Localization loss of the final design's object detection model. The raw data is represented by the faded line and the smoothed data is represented by the bright line.

Localization loss is the next loss metric that is used in object detection tasks in computer vision. Object detection involves both identifying the presence of objects within an image and localizing them with a predictive bounding box. The localization loss calculates any discrepancies between the predicted bounding box coordinates and the true bounding box coordinates. The most common type of localization loss is the mean squared error (MSE) loss, which calculates the squared difference between the predicted and true bounding box coordinates. The localization loss is typically combined with a classification loss to form a joint loss function. The joint loss function is optimized during training to improve the accuracy of the model in detecting and localizing objects within images. While localization loss and classification loss can be the only loss functions utilized to train a model, this can lead to overfitting. In order to prevent overfitting, the model also utilizes regularization loss to train the model. Overfitting occurs when a model becomes too complex and starts to fit the noise in the training data rather than the underlying patterns. Figure 2.10 shows the improvement of the localization loss between the old and new object detection model.

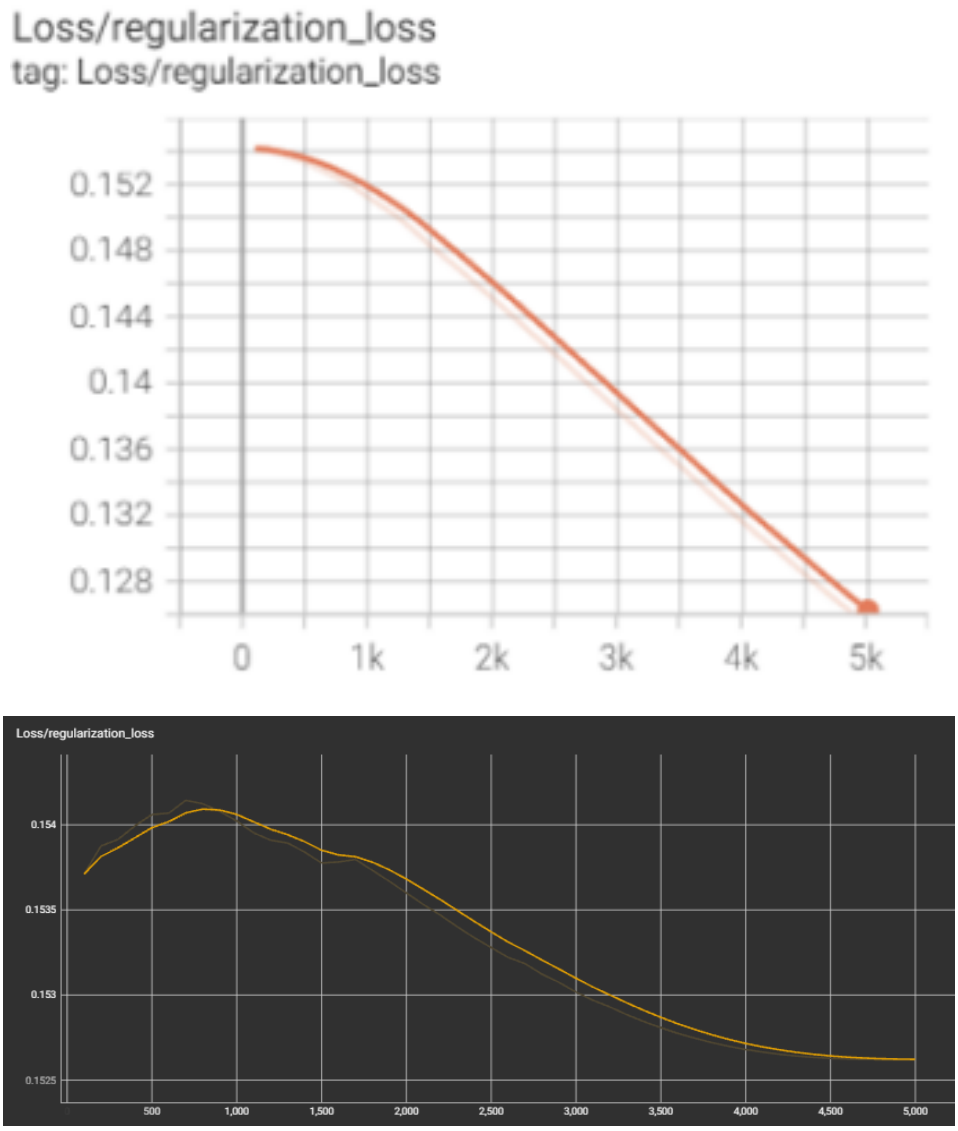

Figure 2.11 Regularization Loss Changes. (a) Regularization loss of the second prototype's object detection model. The raw data is represented by the faded line and the smoothed data is represented by the bright line. (b) Regularization loss of the final design's object detection model. The raw data is represented by the faded line and the smoothed data is represented by the bright line.

Regularization loss is the last loss metric we will be utilizing and is typically added to the overall loss function during training to encourage the model to learn simpler patterns and reduce the impact of noise in the training data. The most common types of regularization loss are L1 and L2 regularization. L1 regularization encourages the model to learn sparse representations by setting some of the weights to zero. L2 regularization encourages the model to learn small weight values and smooth out the decision boundary. The amount of regularization is controlled by a

hyperparameter called the regularization strength, which determines the relative weight of the regularization loss compared to the main loss. Figure 2.11 shows the changes between the old and new object detection model for regularization loss.

(a)

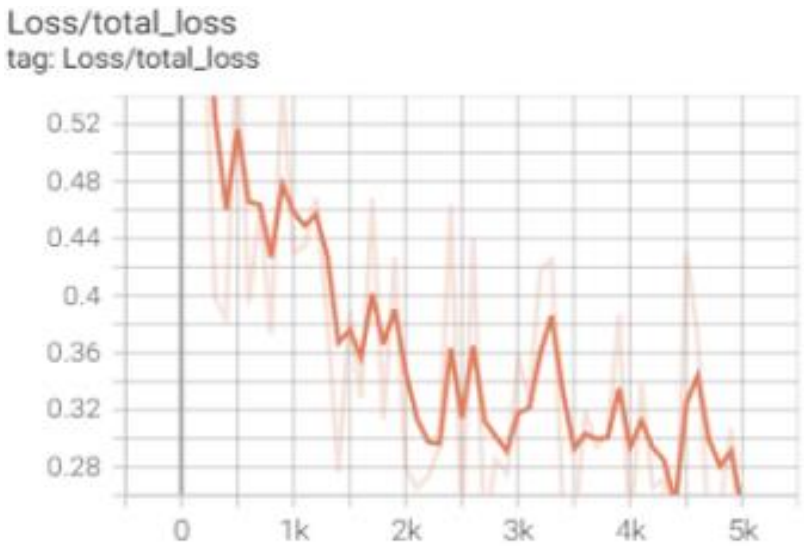

(b)

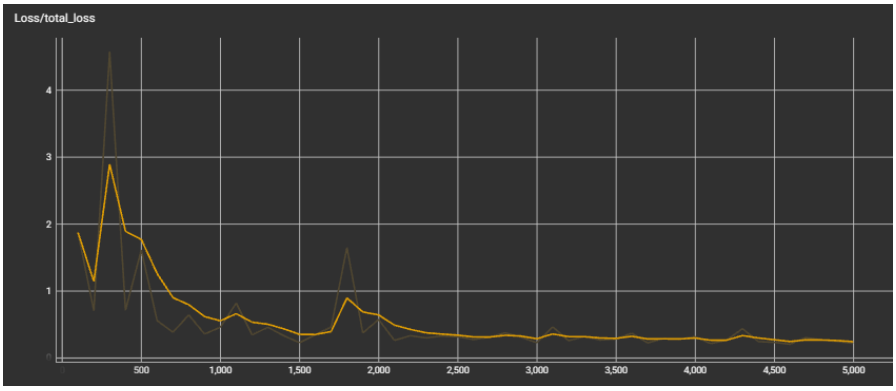

Figure 2.12 Total Loss Changes. (a) Total loss of the second prototype's object detection model. The raw data is represented by the faded line and the smoothed data is represented by the bright line. (b) Total loss of the final design's object detection model. The raw data is represented by the faded line and the smoothed data is represented by the bright line.

Total loss is the sum of all the different types of loss functions used in a machine learning model. For our model, the total loss consists of all three types of loss functions: classification loss, localization loss, and regularization loss. During training, the machine learning algorithm tries to minimize the total loss function by adjusting the mode''s parameters using an optimization

algorithm such as gradient descent. The total loss provides a measure of how well the model is performing on the training data, and the goal is to minimize it as much as possible. The relative weight of each type of loss function in the total loss can be controlled by hyperparameters such as the learning rate and regularization strength. The choice of loss functions and hyperparameters depends on the specific task and the type of model being used. Figure 2.12 shows the improvement of the total loss between the old and new object detection model.

Chapter 3. Results

3.1 Prototype I Results

The first prototype of the headset utilized the Phyphox smartphone application, which granted access to the phone's orientational sensors to output gyroscopic data for the goggles. Since the phone was inserted inside the headset, the smartphone's motion as measured by its sensors was deemed representative of the entire device. Phyphox was selected due to its accessibility on most smartphones, ease of use, and no cost. Nonetheless, using a smartphone as the gyroscopic sensor had a significant drawback: the phone was not entirely secured in place, making it too susceptible to movement for precise measurements. Despite this limitation, it was deemed sufficiently accurate for the first prototype. The primary aim of the first prototype was to develop a preliminary version of the device to validate its feasibility. This approach facilitated the early identification of design flaws such as the sharp and uncomfortable nose notch and the weak strap mount that ultimately broke. Another flaw that surfaced through the initial round of prototyping was the lack of synchronization between the camera and gyroscope. This arose from using two different devices, the smartphone for the gyroscope and accelerometer and Raspberry Pi for the cameras, without enabling communication between the devices. This led to delays between the motion detected by the smartphone and the VOR as detected by the eye-tracking model. Although the data could not assist in any medical diagnosis, the prototype established the feasibility of our device.

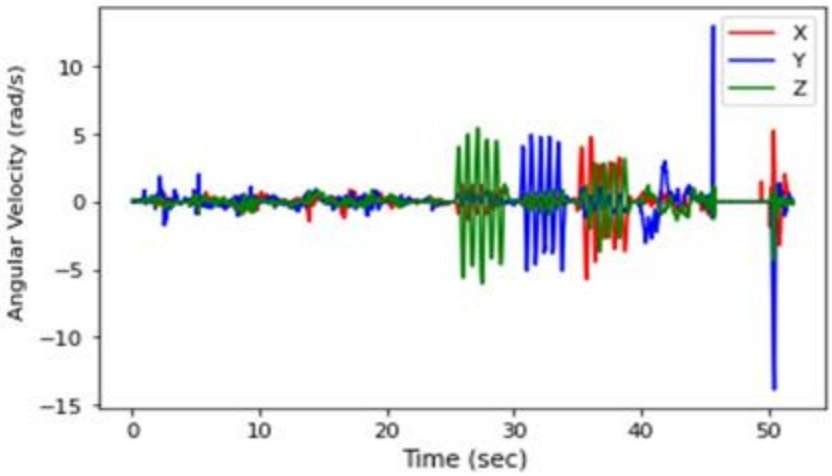

Fig 3.1 Prototype I Gyroscope Results. This figure illustrates the gyroscopic data associated with the movement of the head which in turn moved the goggles. For the first 20 seconds the headset was held as still as possible. Between 20 and 40 seconds, each axis of rotation was tested. X represents roll, Y represents pitch, and Z represents yaw with each letter coinciding with the axis it rotates about.

Figure 3.1 shows the initial data output from rotating the goggles while attached to the head. There was a large amount of noise associated with yaw which we attributed to either difficulty completely isolating the movement, or the iPhone not being as sensitive to yaw rotation as it is to pitch and roll.

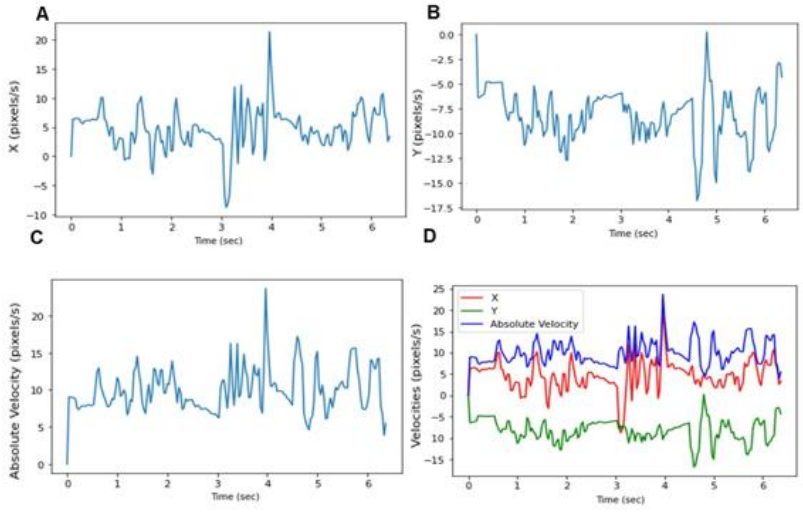

Figure 3.2 Prototype I Pupil Center Tracking A, B) The X- and Y-axis align with the gyroscopic coordinate system and are plotted respectively. C) Plot of the absolute velocity of the pupil center over time. D) Combination of all three plots for ease of comparison

Using the gyroscopic data from Phyphox along with our trained model we were able to gain some preliminary eye-tracking data. This was done by first deriving the center of the pupil. The geometric center of the bounding box represented the center of the pupil. The pupil center of each frame was used to obtain planar velocities based on the pixel location. This was achieved by comparing each frame's pupil center to the previous frame to track how many pixels the center had shifted. The initial experiment was quite simple. The patient was instructed to turn their head to the left then right then center followed by down then up. The results of the experiment can be found in Fig 3.2.

3.2 Prototype II Results

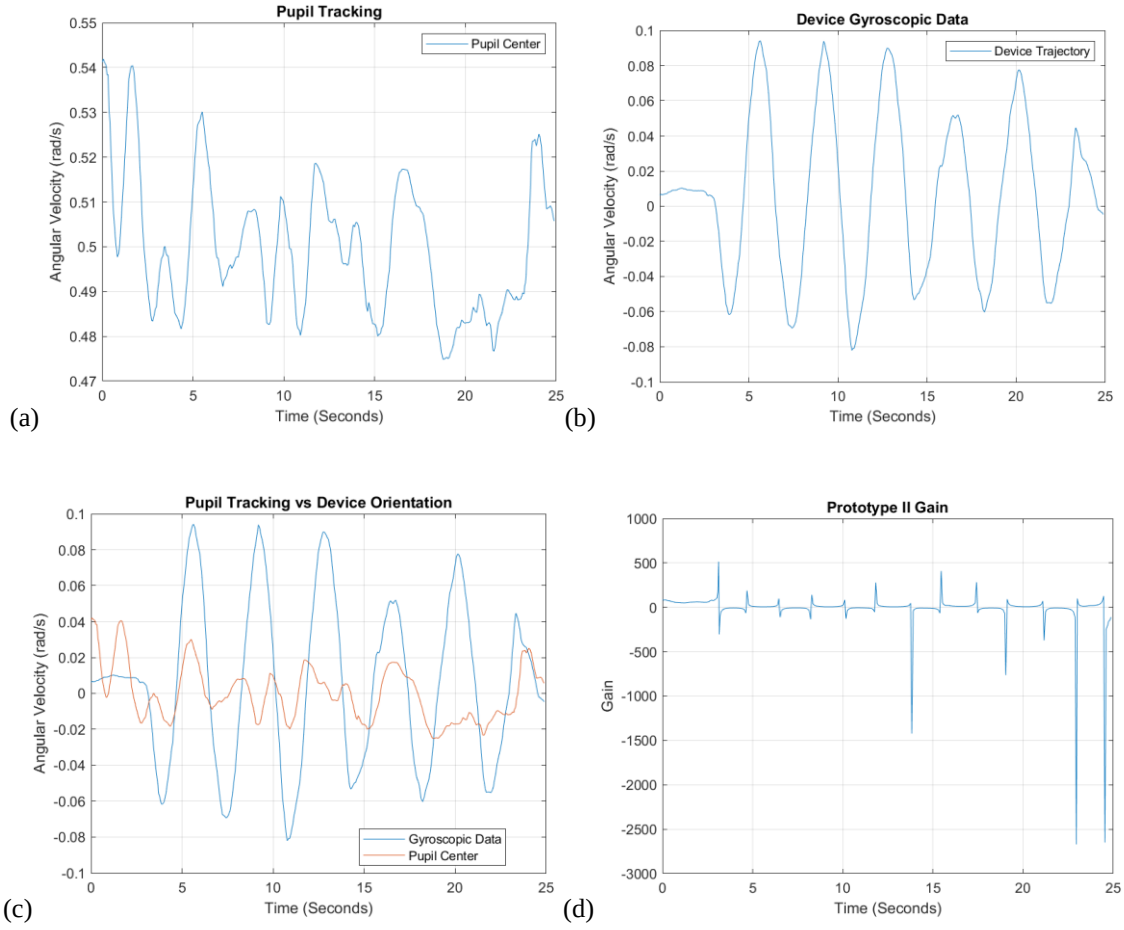

Figure 3.3 Prototype II Pupil Center and Gyroscope Results. (a) Pupil Center tracking over time. (b) Device trajectory tracking over time (c) Pupil Center vs Gyroscopic Trajectory (d) Prototype II Gain

The results of the second prototype are shown in Figure 3.3. In this experiment the subject was asked to keep still for 5 seconds then turn their head right to left for 20 seconds. Figure 3.3a shows the filtered data acquired with prototype II and the object detection model of prototype II. The data was consistently noisy with constant shifts which revealed little data about VOR. This is likely due to the model overfitting based on its training data. Figure 3.3b shows the filtered rotational data acquired with negative and positive velocities relating to turning right and left respectively. Figure 3.3c shows the pupil center and rotational data for ease of comparing the two. The ideal results would show pupil center data similar to the head rotation data. The pupil center and rotational data was found to be positive and weakly correlated with a Pearson correlation coefficient of 0.297. The average gain was found to be -9.282. It is evident that prototype II did not function as intended as it detected a large amount of movement in the first 5 seconds when the subject was completely still. However, this prototype proved that the idea was feasible, and the gyroscope and cameras could be synchronized to yield proper results.

3.3 Final Design Results

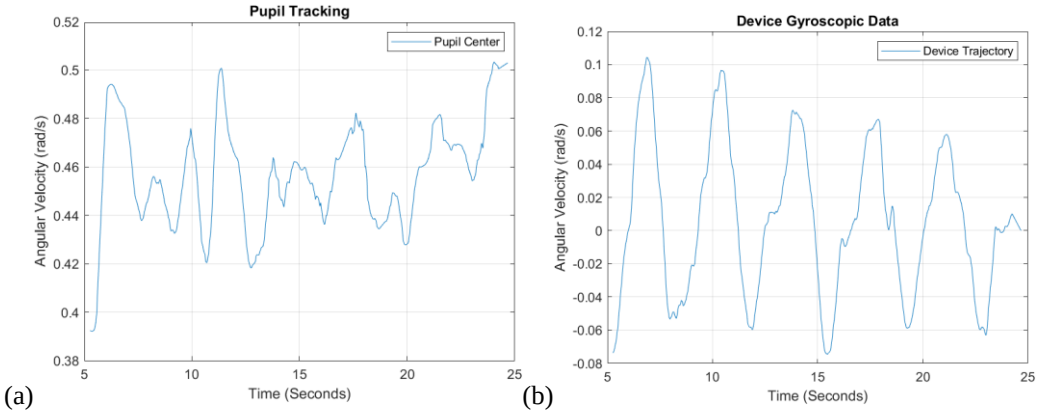

(a) (b)

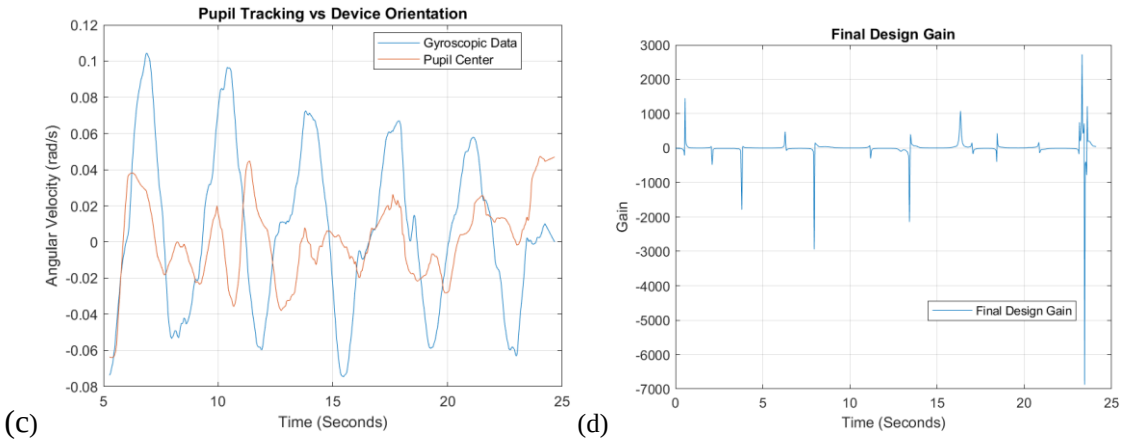

Figure 3.4 Final Design Pupil Center and Gyroscope Results. (a) Pupil Center tracking over time. (b) Device trajectory tracking over time (c) Pupil Center vs Gyroscopic Trajectory (d) Final Design Gain

The results of one trial using the final design are shown in Figure 3.4. Figure 3.4a shows the smoothed data acquired with final design and the final object detection model. The data was considerably less noisy than the pupil center data from prototype II. This is likely due to a combination of improved lighting condition and object detection model. Figure 3.4b shows the smoothed rotational data acquired during the same experimental procedure where the subject was instructed to keep still for 5 seconds then turn their head right and left for 20 seconds. The first 5 seconds were removed to compare only the rotational data, to ensure the gain accuracy was not inflated. Figure 3.4c allows for the comparison between the pupil center and rotational data. While the pupil center does not exactly match the rotational data, it is more similar than prototype II with many more of the peaks aligning. The pupil center and rotational data were found to be negative and weakly correlated with a Pearson correlation coefficient of 0.191. The VOR was estimated by finding gain or the ratio of head rotation to pupil center rotation. The results of 9 trials can be seen in table 3.1. The desired gain is to remain close to one. This is because the VOR is a reflex that causes eye movement in the opposite direction of head motion in order to stabilize gaze. The stabilizing effect causes smooth eye movement in the same direction as head rotation. The average gain for the trial shown in figure 3.4 was found to be 4.478.

Table 3.1 Final Design Correlation and Average Gain.

Trial	Correlation Coefficient	Average Gain
1	-0.019	14.577
2	0.206	3.620
3	0.001	7.573
4	-0.051	24.519
5	0.196	24.719
6	0.191	4.478
7	-0.074	12.882
8	0.050	18.379
9	-0.061	17.026
Averages	0.074	14.419

The correlation and average gain for 9 trials can be seen in table 3.1. The average gain for the final design across all 9 trials was 14.419. The average correlation was 0.074. The large VOR gain values obtained from the study mainly due to absence of de-saccade process to remove huge eye blinks, which cause relatively huge eye movement. The eye motion of saccades should not be counted into the VOR gain computing. Another big potential issue is the synchronization between gyroscope signals and camera image capturing. Even a tiny delay could produce a big VOR computing error.

Chapter 4. Discussion

The purpose of this project was to create a low cost VOG without markers head mounted device that utilizes a machine learning object detection model in order to track head rotation and eye movement. By tracking head rotation and eye movement an individual's VOR can be evaluated by finding gain. Finding an individual VOR gain during head movement will provide additional diagnostic evidence for a myriad of neurological conditions including early onset ataxia, concussion, MS, stroke, and vertigo. The result of the first prototype was a successful proof of concept. It was proven that head rotation and eye movement could be tracked with the use of cameras and a gyroscope. There were several challenges found through the first prototyping process. The first challenge was making the device more comfortable, which was achieved by altering the nose notch and smoothing edges. The other challenge was that the gyroscope and pupil tracking data were not synchronized making it difficult to track gain. This was addressed in the second prototype by adding a gyroscope and accelerometer to the Raspberry Pi. The challenges found during the second prototyping process were noisy data, inadequate lighting conditions, and poor object detection model performance. These challenges were addressed through increased filtering, training steps, training data, and lights. The lights were not only increased in number, but changed to IR. These alterations allowed for much better performance for the final design.

The initial method employed to evaluate the relationship between head rotation and eye movement data involved measuring the correlation between the two datasets. The strength of the correlation indicates how similar the two data sets are and is determined by analyzing the extent to which one variable changes in response to changes in the other variable. The correlation analysis revealed a stronger relationship between head rotation data and eye movement data for the second prototype compared to the final design, yet, both correlations were weak. The average gain for the

final design was also found to be lower for prototype II compared to the final design. However, the second prototype gain calculation contains the first 5 seconds of rest, while the final design does not. It is likely that the inclusion of the 5 seconds of rest inflated the correlation and gain calculations leading to inaccurate true measurements. The reliability of the prototype II is also in question as the sample size is only one. This reduces the statistical power of its results because there is an increased likelihood of random chance affecting the results.

High quality VOG devices such as the ICS Impulse goggles created by GN Otometrics yield VOR gains on average of 0.95 to 1.05. High quality EOG devices such as the one created by Pleshkov and colleagues yield VOR gains on average of 0.92 to 0.97 [15]. When compared to the VOR gains found with the final design of 14.419 it is evident that the device's accuracy needs improvement. However, the ICS Impulse goggles are considerably more expensive than our device. The EOG device used is of a comparable price. Yet, both devices measured VOR gain using an impulse test where the subject turned their head a single time either left or right and the head rotation and eye rotations were recorded. The final design device tracked VOR gain over a longer period of time with an average of 5 full head rotation from left to right. This is likely why our device has such a considerably less accurate VOR gain measurements.

The sources of error in our experiment are thought to be from the device shifting on the head, the gyroscope drifting over time, and object detection model errors. While the device became more comfortable with the nose notch improvements, the extra space allotted allowed for more slippage if the device was not held securely. This is likely why some of the average VOR gain measurements were as high as 25. While the drifting of the gyroscope was mitigated with the inclusion of accelerometer data to create a complementary filter, the value likely slightly drifts over the 25 seconds of measurement contributing to inaccurate results. The last source of error

likely stems from the object detection model. While the model is highly accurate even when the eye shifts far from the center, errors still occur when the eye blinks. When the eye blinks, the model can lose the pupil center as eye lashes and the eye lid block part of or all of the eye. This is a significant source of error as it was difficult for the subjects to keep their eyes open for the entire 25 seconds. Another small source of error is how focused the eye is during the test. The subjects were not instructed how or where to focus on during the experiment as the focus was to try to keep their eyes open and look forward. Eye movement is affected by if the eye is focused or relaxed, so in future studies the subjects should be instructed to relax and not focus their eye during testing to mitigate this source of error.

While significant improvements were made from the first prototype to the final design, the device is far from complete. The first improvement to be made is finding a more accurate pupil center than the center of the bounding box. This is necessary because if the bounding box's edges are not perfectly aligned with the edges of the iris, which tends to happen as the pupil shifts further from the center, the eye tracking data is less accurate and more prone to noise. One solution to improve accuracy would be to search for an ellipse within the bounding box. The ellipse would represent the pupil and be found by comparing color intensities inside the bounding box. The idea behind using color intensities is that the pupil is much darker than the surrounding iris so a clear border can be found. Once the ellipse was fit, the center was easily procured by finding the geometric center of the ellipse. The geometric center of the ellipse would be a more accurate representation of the pupil center which would improve the overall accuracy of the device. The next improvement to be made is to track the torsional component of eye movement. This is a particularly complex problem that has no easy solution. One solution could be to train the object detection model to find a prominent vein in the scleral, or white part of the eye, and track its

rotation. However, not all eyes have prominent veins or if they do, they can be lost throughout eye movement. The camera quality would also have to improve to be able to consistently track the veins, which would cause additional costs. Future experiments should also be conducted on diseased individuals since testing has only been conducted on a young and healthy population. This would allow for the comparison of healthy to diseased VOR gains.

Table 4.1. Price Breakdown of the Device.

Part	Cost (Dollars)
Raspberry Pi 4 model B/8GB	75.00
Micro-HDMI to HDMI Cable	5.00
Raspberry Pi HQ Camera CS	50.00
2.8 -12mm Varifocal C-mount Lens	64.99
Gyroscope	24.20
Fan	12.10
IR light x2	20.40
3D Printed Headset	39.40
Wire Connectors	6.80
Total Price	297.89

Presently, there are numerous eye trackers accessible in the market with prices ranging between roughly 300 to 30,000 US Dollars. The majority of the cost does not stem from the hardware itself as there has been a significant decrease in the cost of high-quality digital camera technology over the past decade. The expenses are primarily attributed to the customization of software implementation. The eye trackers that cost less than 1000 US Dollars are mostly remote eye tracking devices that track gaze on a screen but are not capable of tracking VOR. The device created through this project cost only 297.89 US Dollars making it one of the cheapest devices on the market. The breakdown of the prices of all the equipment used can be found in table 4.1. The price could be further reduced in the manufacturing process as each of these parts was bought individually.

Chapter 5. Conclusion

In conclusion, the purpose of this project was to create a low-cost vestibulo-ocular reflex (VOR) device using machine learning object detection to track head rotation and eye movement without markers. This device has potential diagnostic applications for a variety of neurological conditions, including concussion, early onset ataxia, MS, stroke, and vertigo. While the first prototype was a successful proof of concept, challenges arose, including making the device more comfortable, synchronizing gyroscope and pupil tracking data, noisy data, inadequate lighting conditions, and poor object detection model performance. These challenges were addressed in the second prototype through increased filtering, training steps, training data, and improved lighting conditions. Despite these improvements, there were still sources of error, including the device shifting on the head, gyroscope drifting over time, and object detection model errors. The device's accuracy needs further improvement when compared to high-quality VOG and EOG devices. While high-quality VOG devices are more accurate, they are also more expensive. The device needs improvements such as finding a more accurate pupil center and implementing 3D torsional tracking. Overall, this project has great potential for future research and development with the potential of creating a low-cost alternative for diagnostic and clinical applications.

Chapter 6. Other Project

A Head Tilting Scheme to Detect Small Amount of Middle Ear Effusion

6.1 Abstract:

Otitis media (OM) is a common condition in young children, characterized by the presence of fluid in the middle ear cavity. Diagnosis of fluid buildup in the middle ear is typically performed using a pneumatic otoscope, which is dependent on the severity of middle ear effusion (MEE) and can lead to subjective diagnoses. In this study, we propose that the position of MEE changes when the head is tilted 30°, and that this change induces motion in the tympanic membrane (TM) in response to sound stimuli, which can be detected by a scanning laser Doppler vibrometer (SLDV) using our new computer-aided detection (CAD) scheme.

To test this hypothesis, we simulated MEE in five human temporal bones and measured TM displacement in response to sound stimuli in a 30-degree tilting experiment. We analyzed the effects of head tilting on TM motion changes statistically. Our results indicate that the average sound displacement across the bottom half of the TM between the frequency bands of 0.8 kHz to 6.5 kHz in the tilted position was significantly lower than in the normal (non-tilting) position. This finding provides a practical application of quantitative assessment for diagnosing OME. The new tilting approach combined with the new algorithm offers a less subjective and more reliable process to detect small MEE.

In summary, our study demonstrates the potential of using a tilting approach combined with a CAD scheme and SLDV to detect MEE more objectively and accurately. This approach could provide a more reliable diagnosis for OME and improve clinical decision-making.

6.2 Introduction

Otitis media (OM) is a common condition among young children, characterized by the presence of fluid in the middle ear cavity. It is the top reason for children to visit a physician, and the usual treatment is prescription antibiotics, which contributes to children in developed countries spending approximately 90 days on antibiotics by the age of two [37-40]. This is problematic as many pathogenic bacterial species have become resistant to antibiotics, and the excessive prescription of antibiotics may lead to more bacteria evolving to become resistant [41-43]. The World Health Organization has declared this problem a threat to modern medicine, highlighting the need for a more accurate diagnosis of OM.

The current tool for detecting fluid buildup in the middle ear is the pneumatic otoscope, which relies heavily on the severity of the buildup and leads to a subjective diagnosis [44-50]. Otoscopy or tympanometry is very difficult to detect MEE in cases where the amount is small, or the MEE is below the lower limit of the TM. We hypothesize that MEE will move in the middle ear cavity due to gravity when the head is tilted 30° laterally. Furthermore, we expect that the change in MEE position will cause a change in middle ear impedance, which will, in turn, cause a change in TM motion in response to sound stimuli. Using SLDV, the change in TM motion will be detected, and our recently developed CAD scheme can quantify the change.

Our study aims to improve the accuracy of diagnosing small MEEs in OM. By developing a more accurate prediction of small MEEs, otologists can make more accurate diagnoses of OM, which will lead to a reduction in the excessive prescription of antibiotics. This, in turn, can contribute to the reduction of antibiotic-resistant bacteria and prevent the further evolution of antibiotic-resistant bacterial strains.

6.3 Methods:

Overall approach:

Small amount of MEE was simulated by 0.1ml saline injection into the five human temporal bones (TB). SLDV and wide band tympanometry (WBT) were used to measure the middle ear impedance before and after injection under control and tilting setups.

Wide band tympanometry measurement

An Interacoustics Titan tympanometer (Version 3.4.0) was used to measure the impedance change in response to MEE. The measurements procedure was described in our previous study (ref). WBT measures were performed four times in setup and averaged to minimize influence of physical movement of the TBs during the measurement setup changes. A full WBT absorbance dataset is characterized in three parametric dimensions (e.g., absorbance, frequency, and pressure). For the present analysis, a single absorbance spectrum at a fixed tympanometric pressure was selected for each test position setup. The chosen fixed tympanometric pressure was the pressure at which absorbance measures at 226 Hz peaked, which corresponds to maximum tympanic membrane compliance in conventional, single frequency tympanometry.

SLDV measurement

MEE was replicated by injecting a small amount (0.1ml) fluid into the middle ear of the human cadaver ear. The human cadaver ear was initially inspected by an operating microscope (OPMI-1, Zeiss, Thornwood, NY) to ensure a normal structure. A silicone catheter was inserted through the bony part of the Eustachian tube and into the middle ear canal (MEC). Once the tip was confirmed to reach the MEC it was fixed in place. A second hole was drilled near the arcuate eminence and

into the MEC. A second catheter was inserted through this hole for outflow. This was done to ensure pressure equilibrium when injected fluid through the first catheter.

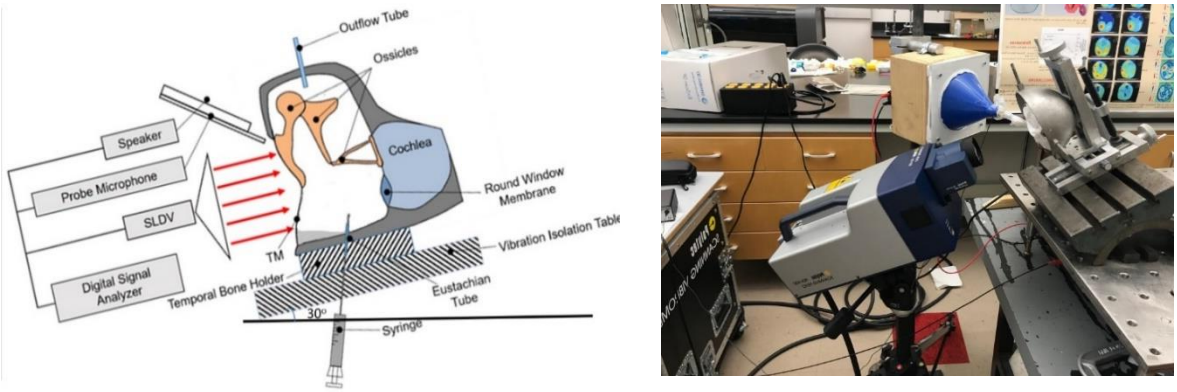

Figure 6.1 Experimental Setup (a) Schematic of the experimental setup not tilted. The human ear is held in place on the tilting milling table which is attached to the vibration isolation table. The laser, speaker, amplifier, and microphone are then directed at the external auditory meatus (b) Picture of the experimental setup. The human cadaver ear is held in place via three pins. The holding device is locked into the tilting milling table which is locked into the vibration isolation table. The SLDV with the TDT CF1 speaker and RCA SA-155 amplifier are pointed at the external auditory meatus. The SLDV is a grey and blue device with a lens. The speaker and amplifier are housed in the box with the blue funnel extended.

The human ear is held in place on the tilting milling table which is attached to the vibration isolation table. The laser, speaker, amplifier, and microphone are then directed at the external auditory meatus B) Picture of the experimental setup. The human cadaver ear is held in place via three pins. The holding device is locked into the tilting milling table which is locked into the vibration isolation table. The SLDV with the TDT CF1 speaker and RCA SA-155 amplifier are pointed at the external auditory meatus. The SLDV is a grey and blue device with a lens. The speaker and amplifier are housed in the box with the blue funnel extended.

Next, we placed the TB holder on the tilting milling table to achieve the desired tilt of 30° laterally. The SLDV was then adjusted to the same angle with double laser alignment. The tilting milling table was secured on top of a vibration isolation table. Once set-up was complete, a 90dB

chirp stimulus from 0.2 to 8 kHz generated by a function generator (HP 35670A, Hewlett-Packard, Palo Alto, CA) and an amplifier (RCA SA-155, Radio Shack, Fort Worth, TX) was delivered to the TM by a speaker (TDT CF1, Tucker-Davis Technologies, Alachua, FL) via the external auditory meatus. Then the full-field surface motion of the tympanic membrane was recorded by the SLDV (PSV-400, Polytec Inc., Irvine, CA) with its corresponding software package (PSV 8.8, Polytec Inc., Irvine, CA). This entire process took 15 minutes and resulted in 125 data points.

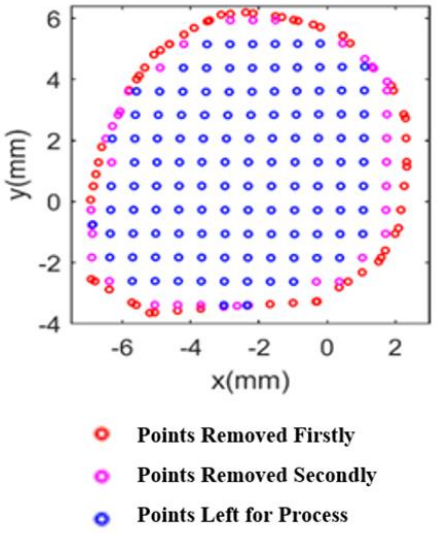

Figure 6.2. Scanning Point Removal. Illustration of scanning points removed of outermost scanning points 2 times successively across the TM

The experiment was conducted on the ear in four different variations: no liquid injected in an upright position, no liquid injected in a tilted position, liquid injected in an upright position, and liquid injected in a tiled position. All positions were then compared using an algorithm to process the raw data exported from PVS 8.8. For each frequency, the coordinates of all scanning points and the corresponding displacement were saved. The first part of the algorithm removed the outermost layer of scanning points twice to ensure all the points are located on the TM as seen in figure 2.

Next, we utilized a robust smoothing algorithm [48] to reduce experimental noise. Then an analysis of variance (ANOVA) was conducted on the smoothed data, comparing the mean sound

displacement of all four variations of the experiment. The ANOVA test results in an F-statistics that reveal if the data is significantly different. Then the surface variation and area to volume ratios were calculated to compare the effects tilting had.

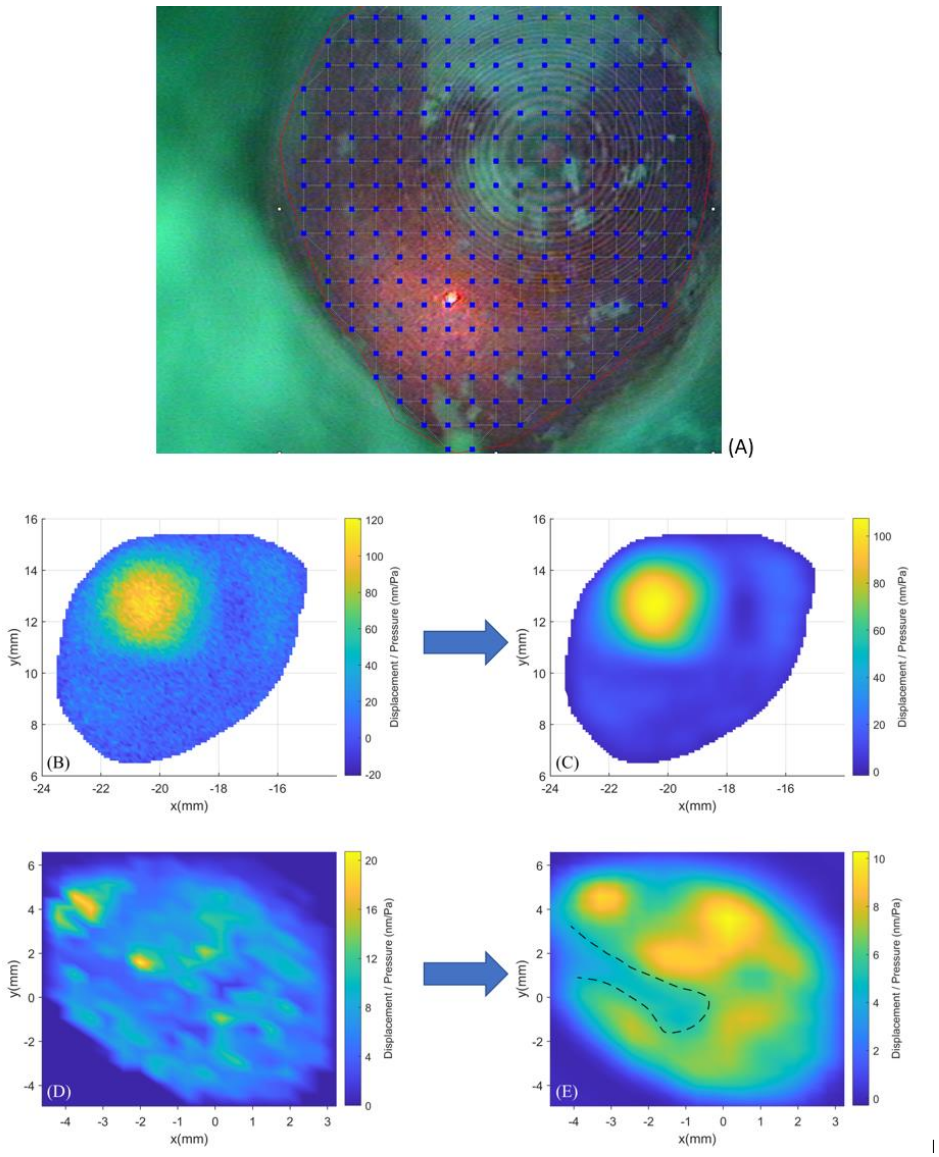

Figure 6.3. Illustration of the Data Preprocessing, which shows (a) the removal of outermost scanning points on TM for 2 times successively, (b) FE simulation derived deflection shape with a Gaussian distribution noise, (c) FE simulation derived deflection shape after smoothing, (d) deflection shape of TM at 1381.25 Hz before smoothing, and (E) deflection shape of TM at 1381.25 Hz after smoothing.

6.4 Results:

The tympanometry measurements showed highly similar results among control, 0.1ml MEE in normal position and 0.1 ml MEE in 30-degree tilting position as shown in Figure 6.3

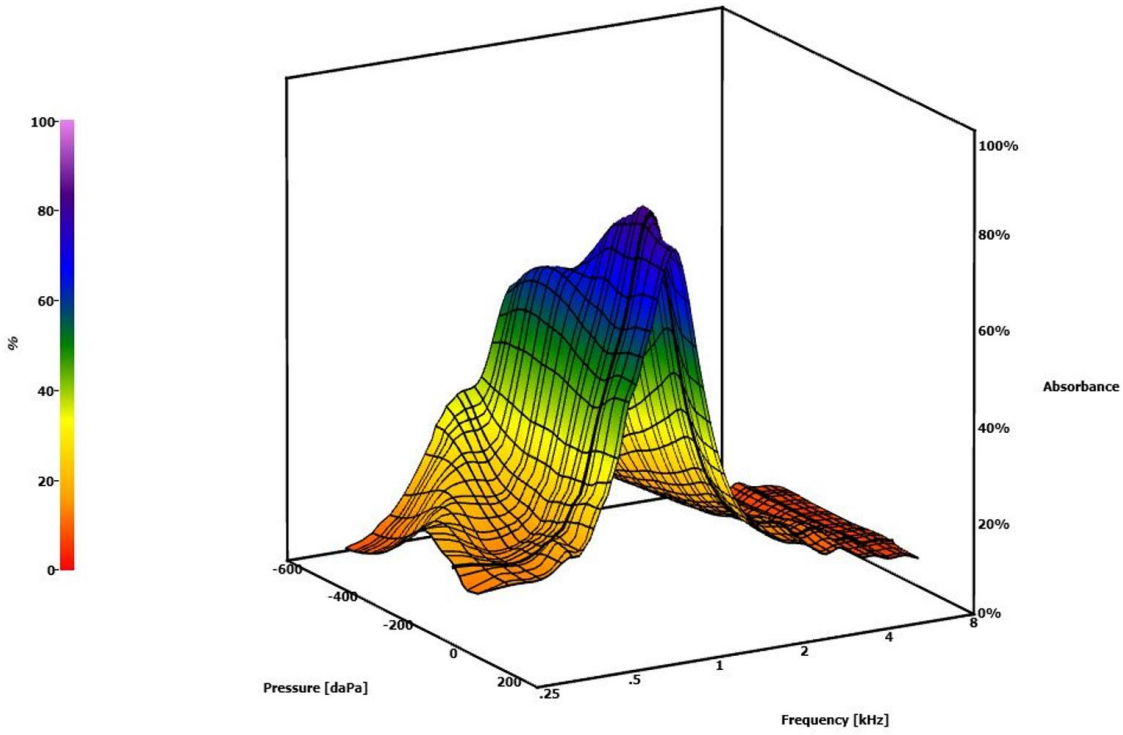

Figure 6.4. TB Tympanometry Measurements. A sample of 3D tympanometry gram from TB measurements

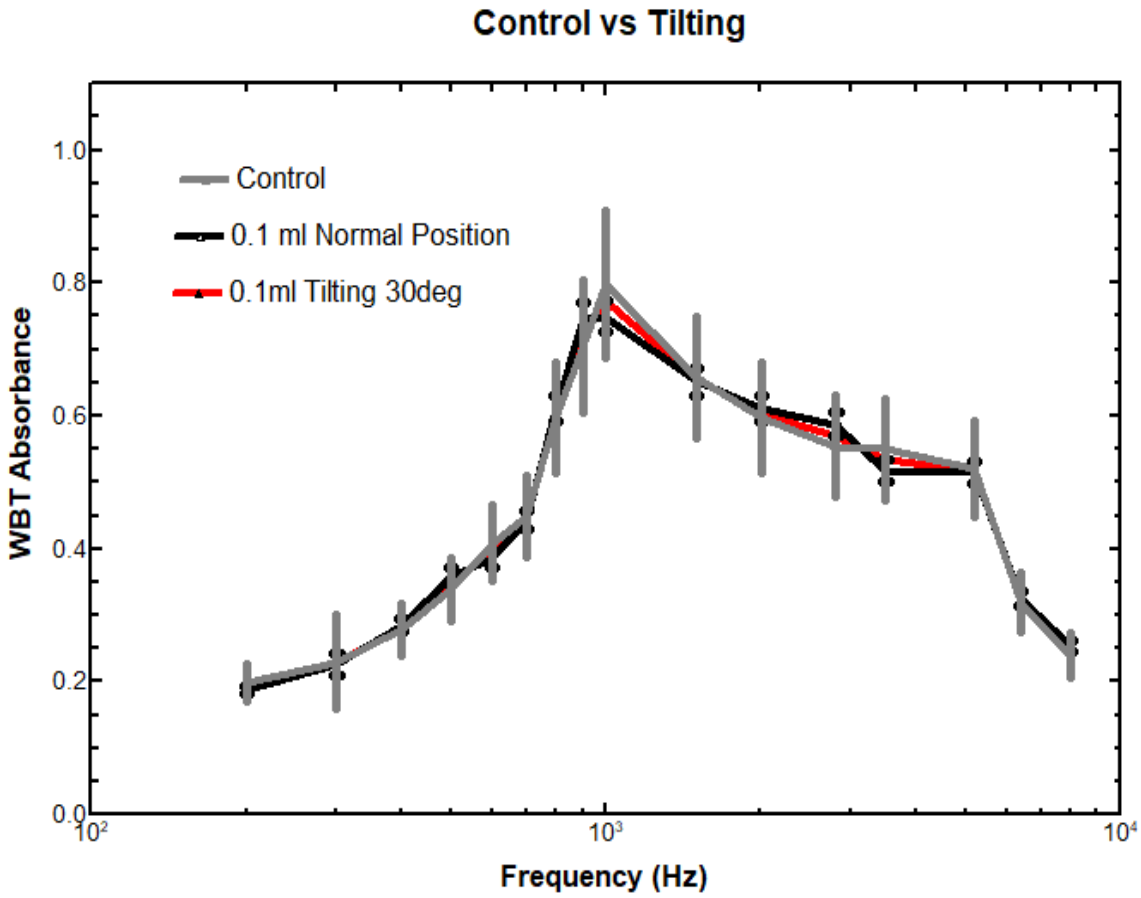

Figure 6.5. Pre and Post Injection Absorbance Averages. This figure compares the pre and post injection grand averages for the absorbance in cadaver ears. Confidence bands (95%) are shown for each grand average and are based on a t distribution due to the small sample size of N = 5 (df = 4), t = 2.571. The * range approximately indicates the frequency region (about 0.6–1.1 kHz) over which pre- and post-injection absorbance differs significantly ($p < 0.05$) based on the degree of overlap of the confidence bands (19). The maximum average effect occurred at 1 kHz with absorbance decreasing from ~0.8 to ~0.5 after MEE formation. As expected for a longitudinal control comparison, no significant differences were observed between the pre- and postoperative WBT patterns in five temporal bones.

This preliminary study tested the effects that tilting the head laterally had on the detection of otitis media in the middle ear cavity. When the displacements across all frequencies were averaged and compared, they yielded no significant difference. This led to narrowing the frequency range to 0.8 to 6.5 kHz. We chose this range according to where Figure 2a seemed to have the largest difference and least amount of noise.

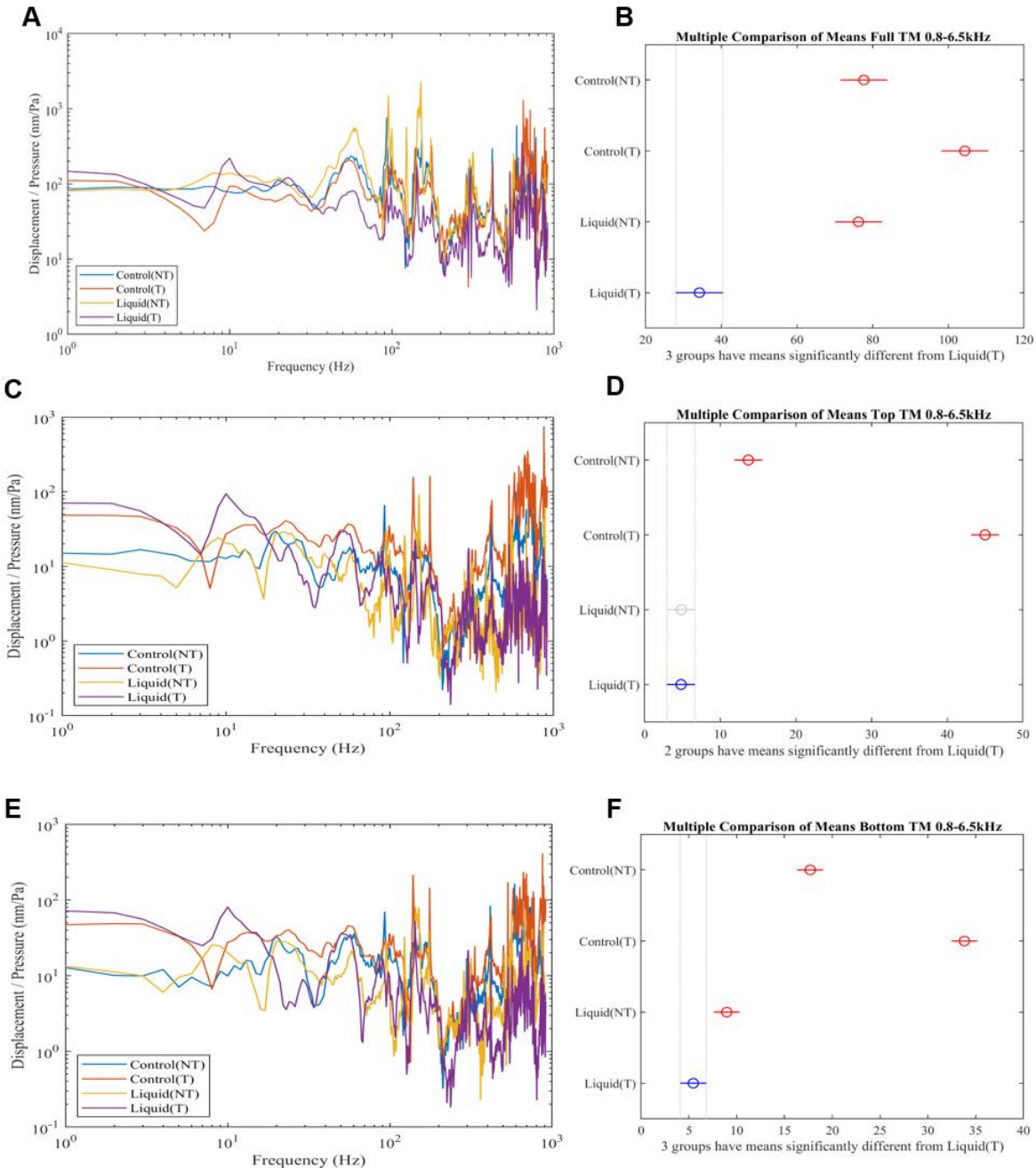

Figure 6.6. Comparison of Sound Displacements

A) Sound displacement results across the frequencies 0.8 to 6.5kHz across the full TM

B) ANOVA test results of full TM

C) Sound displacement results across the frequencies 0.8 to 6.5kHz across the Top half of the TM

D) ANOVA test results of Top half of the TM

E) Sound displacement results across the frequencies 0.8 to 6.5kHz across the bottom half of the TM

F) ANOVA test results of Bottom half of the TM

Initially, we began by looking at the full surface of the TM, but this yielded no significant difference between normal positions with and without liquid as shown in Figure 2b. We believed this to be caused by gravity pulling the fluid away from the top of the TM, causing the average to be skewed. We then proposed to look exclusively at the bottom half of the TM since this is where the media should be forced once the head is tilted. The division of the TM can be seen in Figure 6.6. When we ran the ANOVA test comparing exclusively the bottom half of the TM, the results, shown in Figure 6.5D, indicated that the average sound displacement between the frequency bands .8 kHz to 6.5 kHz of the tilted head was significantly lower than that of the controls and liquid-filled ear in the normal position. The lower sound displacement is to be expected due to the fluid exerting pressure on the TM reducing its ability to vibrate and lowering its response.

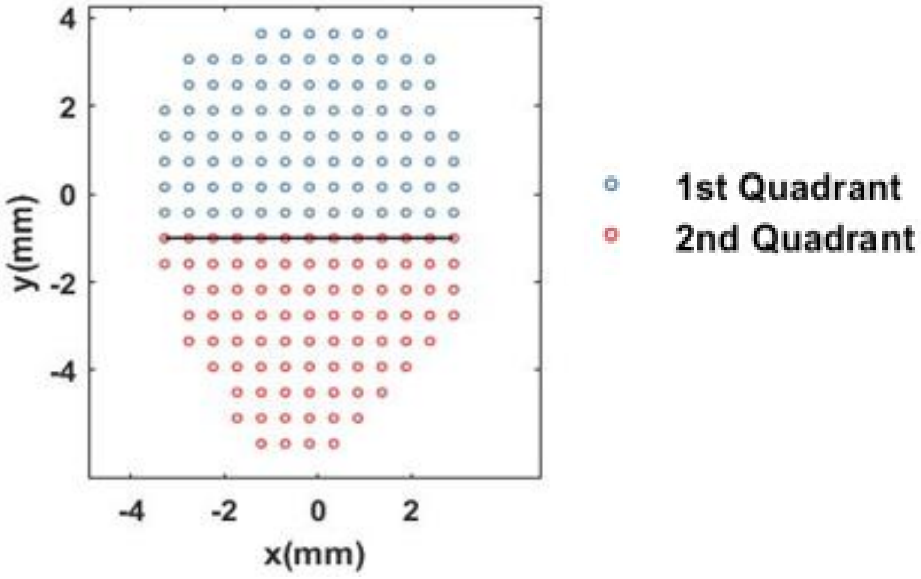

Figure 6.7. TM Quadrant Division. Illustration of the division of the TM into two halves

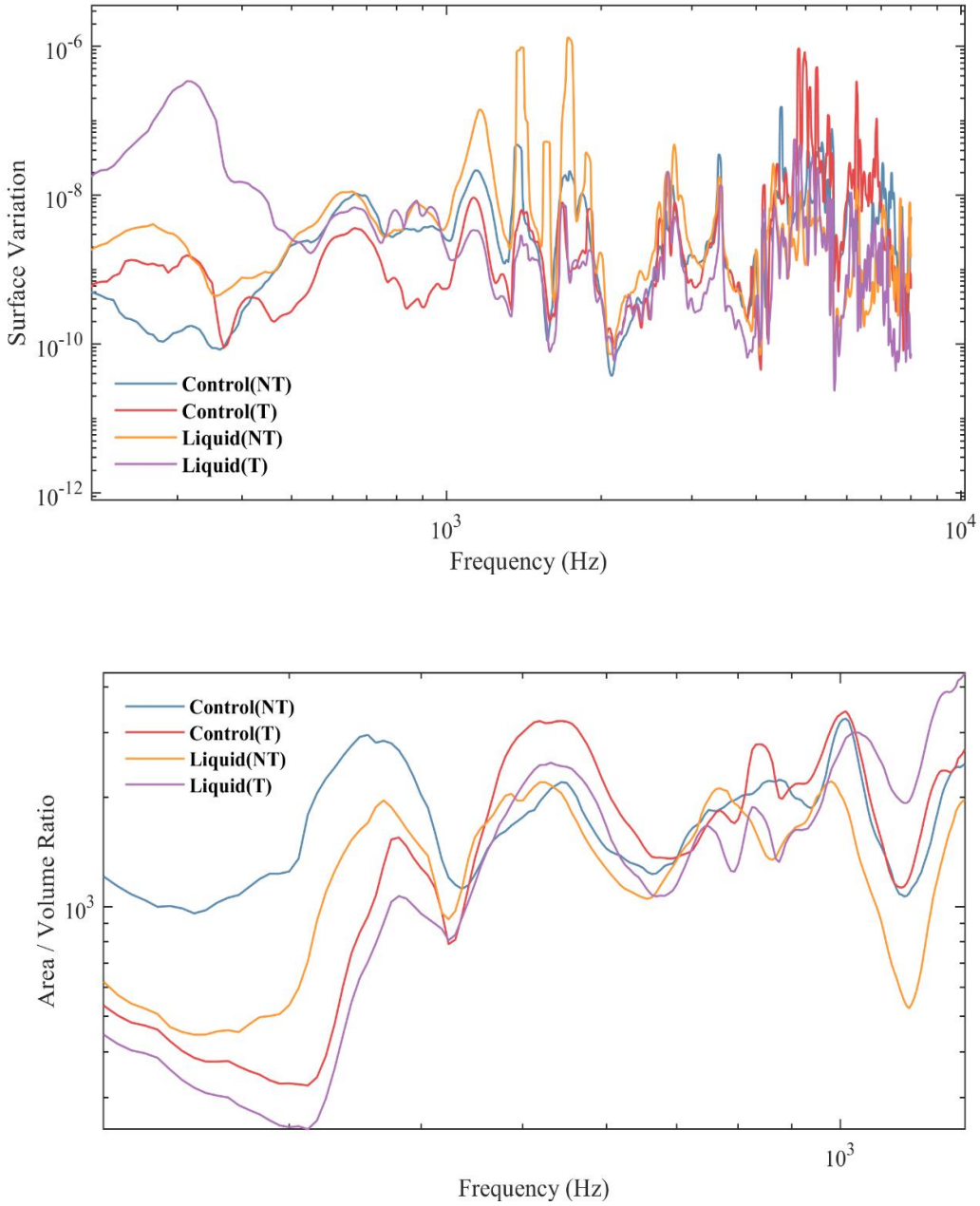

Figure 6.8. Surface Variation and Area to Volume Ratio Results. (a) Surface variation of each trial across the frequencies 0.2 to 6.5 kHz in the bottom half of the TM (b) Area to Volume Ratio of each trial across the frequencies 0.2 to 6.5 kHz in the bottom half of the TM.

The surface variation and area-volume ratio quantitatively describe the degree of TM deformation and complexity of the TM surface deflection shape, respectively. The surface variation was higher for the liquid trials than the control trials at low frequencies, as seen in figure

5a, suggesting it is a valuable indicator of OME. At low frequencies, as seen in figure 5b, the area to volume ratio for the liquid tilting trial was the lowest, and at high frequencies was the greatest. This suggests that tilting causes greater variance in the area to volume ratio, which is another valuable indicator of OME.

6.5 Discussion:

Middle ear effusion is characteristic of otitis media and it has been always challenges for physicians when the MEE is small or below the bottom edge of TM annual. The present study tried to modify a routine clinical setup with a 30 degree tilting head using a SLDV measurement to detect small amount of MEE. Processed the raw data with a newly developed CAD scheme, the small amount of MEE (e.g. 0.1 ml) was successfully detected when wide band tympanometry failed. These preliminary yet promising results bring hope for early detection of OM/OME even the inflammation is not obvious.

Many previous studies try to quantify the middle ear mechanics change in response to MEE and the sensitivities of TM motion change was successfully detected when MEE is substantial with quite a few approaches, such as SLDV, holograph, wide band tympanometry, or OCT [47-49]. However, when MEE amount is small, it is very difficult to observe or measure the change of middle ear change, morphologically or mechanically with routine setup while the subject stands as normal posture. We hypothesize the tilting of the head will change the location of MEE inside the middle ear cavity and the impedance of middle ear or the TM motion in response to sound stimuli will be changed. The data measured from five human temporal bones confirm the TM motion changed with tilting setup and our recently established CAD scheme detected the difference, especially in the lower part of the TM.

Future Study

The present study indicates that a SLDV with a CAD scheme can detect a small amount of MEE in a tilting setup. This approach is feasible to be used in clinical applications in future with promising outcomes in this preliminary study. The feasibility of application of this setup with OCT scanning since OCT is more and more common in clinics.

6.6 Conclusion:

In this study, we tested a tilting paradigm to detect small amount of middle ear effusion with SLDV measurements in five human TBs. The new tilting approach amalgamated with our algorithm offers a less subjective and more reliable process to detect MEE. A more effective diagnosis leads to more effective treatment, which should lead to fewer antibiotics prescribed. The benefit this technique provides over the pneumatic otoscope could outweigh the significantly higher cost of the machine itself. The high cost of the machine indicates it would be more effectively implemented in wealthy nations, which are the most responsible for the over-prescription of antibiotics. For future studies, different angles could be tested to find the optimal test angle.

References:

1. Robert J.K. Jacob, Keith S. Karn, Commentary on Section 4–- Eye Tracking in Human-Computer Interaction and Usability Research: Ready to Deliver the Promises, The Min''s Eye, North-Holland, 2003, Pages 573-605, ISBN 9780444510204, https://doi.org/10.1016/B978-044451020-4/50031-1.
2. Drewes, Heiko. (2010). Eye Gaze Tracking for Human Computer Interaction.
3. Chang WD. Electrooculograms for Human-Computer Interaction: A Review. Sensors (Basel). 2019 Jun 14;19(12):2690. doi: 10.3390/s19122690. PMID: 31207949; PMCID: PMC6630230.
4. Zhang X, Liu X, Yuan SM, Lin SF. Eye Tracking Based Control System for Natural Human-Computer Interaction. Comput Intell Neurosci. 2017;2017:5739301. doi: 10.1155/2017/5739301. Epub 2017 Dec 18. PMID: 29403528; PMCID: PMC5748315.
5. Vessoyan K, Steckle G, Easton B, Nichols M, Mok Siu V, McDougall J. Using eye-tracking technology for communication in Rett syndrome: perceptions of impact. Augment Altern Commun. 2018 Sep;34(3):230-241. doi: 10.1080/07434618.2018.1462848. Epub 2018 Apr 27. PMID: 29703090.
6. Hwang CS, Weng HH, Wang LF, Tsai CH, Chang HT. An eye-tracking assistive device improves the quality of life for ALS patients and reduces the caregiver'' burden. J Mot Behav. 2014;46(4):233-8. doi: 10.1080/00222895.2014.891970. Epub 2014 Apr 14. PMID: 24731126.
7. Li J, Chen Z, Zhong Y, Lam HK, Han J, Ouyang G, Li X, Liu H. Appearance-Based Gaze Estimation for ASD Diagnosis. IEEE Trans Cybern. 2022 Jul;52(7):6504-6517. doi: 10.1109/TCYB.2022.3165063. Epub 2022 Jul 4. PMID: 35468077.
8. Snegireva N, Derman W, Patricios J, Welman KE. Eye tracking technology in sports-related concussion: a systematic review and meta-analysis. Physiol Meas. 2018 Dec 21;39(12):12TR01. doi: 10.1088/1361-6579/aaef44. PMID: 30523971.
9. Lev, A., Braw, Y., Elbaum, T., Wagner, M., & Rassovsky, Y. (2022). Eye Tracking During a Continuous Performance Test: Utility for Assessing ADHD Patients. Journal of Attention Disorders, 26(2), 245–255. https://doi.org/10.1177/1087054720972786
10. Atchison, D. (n.d.). Optics of the Human Eye. Lecture, Queensland University of Technology; Queensland University of Technology. 2021.
11. Human eye. The European Space Agency (ESA). (n.d.). Retrieved April 14, 2023, from https://www.esa.int/ESA_Multimedia/Images/2014/11/Human_eye
12. Dunbar, B. (2004, February 26). Human vestibular system in Space. NASA. Retrieved April 14, 2023, from https://www.nasa.gov/audience/forstudents/9-12/features/F_Human_Vestibular_System_in_Space.html

13. Bronstein AM, Patel M, Arshad Q. A brief review of the clinical anatomy of the vestibular-ocular connections-how much do we know? Eye (Lond). 2015 Feb;29(2):163-70. doi: 10.1038/eye.2014.262. Epub 2014 Nov 21. PMID: 25412719; PMCID: PMC4330278.
14. Kingma H, van de Berg R. Anatomy, physiology, and physics of the peripheral vestibular system. Handb Clin Neurol. 2016;137:1-16. doi: 10.1016/B978-0-444-63437-5.00001-7. PMID: 27638059.
15. Pleshkov M, Zaitsev V, Starkov D, Demkin V, Kingma H, van de Berg R. Comparison of EOG and VOG obtained eye movements during horizontal head impulse testing. Front Neurol. 2022 Sep 2;13:917413. doi: 10.3389/fneur.2022.917413. PMID: 36119710; PMCID: PMC9479731.
16. Singh, Hari. (2012). Human Eye Tracking and Related Issues: A Review. International Journal of Scientific and Research Publications. 2. 1-9.
17. Chronos Vision. (n.d.). Scleral Search Coils 2D/3D. Retrieved April 14, 2023, from https://www.chronos-vision.de/downloads/CV_Product_SSC.pdf
18. Dunbar, B. (2004, February 26). Human vestibular system in Space. NASA. Retrieved April 14, 2023, from https://www.nasa.gov/audience/forstudents/9-12/features/F_Human_Vestibular_System_in_Space.html
19. Liang J, Luong V, McCraw J, Schroeder A, Zhang K, Gan R, Dai C. A novel 3D video oculography system for measuring cross-axis vestibulo-ocular reflex. Med Eng Phys. 2021 Oct;96:41-45. doi: 10.1016/j.medengphy.2021.08.007. Epub 2021 Aug 27. PMID: 34565551.
20. Larrazabal AJ, García Cena CE, Martínez CE. Video-oculography eye tracking towards clinical applications: A review. Comput Biol Med. 2019 May;108:57-66. doi: 10.1016/j.compbiomed.2019.03.025. Epub 2019 Mar 30. PMID: 31003180.
21. Kothari RS, Chaudhary AK, Bailey RJ, Pelz JB, Diaz GJ. EllSeg: An Ellipse Segmentation Framework for Robust Gaze Tracking. IEEE Trans Vis Comput Graph. 2021 May;27(5):2757-2767. doi: 10.1109/TVCG.2021.3067765. Epub 2021 Apr 15. PMID: 33780339.
22. Yu L, Liu H, Pi X, Chen W, Xu S, Yan X. [Research on Exact Location Algorithm of Pupil Center Based on Ellipse Fitting]. Zhongguo Yi Liao Qi Xie Za Zhi. 2017 May 30;41(3):170-174. Chinese. doi: 10.3969/j.issn.1671-7104.2017.03.004. PMID: 29862760.
23. De Kloe YJR, Hooge ITC, Kemner C, Niehorster DC, Nyström M, Hessels RS. Replacing eye trackers in ongoing studies: A comparison of eye-tracking data quality between the Tobii Pro TX300 and the Tobii Pro Spectrum. Infancy. 2022 Jan;27(1):25-45. doi: 10.1111/infa.12441. Epub 2021 Oct 22. PMID: 34687142.
24. Sun H, Wang Y, Jiang H, Gao Z, Wu H. The clinical application of head-shaking test combined with head-shaking tilt suppression test in distinguishing between peripheral and central vertigo at

bedside vs. examination room. Braz J Otorhinolaryngol. 2022 Nov-Dec;88 Suppl 3(Suppl 3):S177-S184. doi: 10.1016/j.bjorl.2022.03.003. Epub 2022 May 20. PMID: 35760753; PMCID: PMC9760989.

25. Nham B, Reid N, Bein K, Bradshaw AP, McGarvie LA, Argaet EC, Young AS, Watson SR, Halmagyi GM, Black DA, Welgampola MS. Capturing vertigo in the emergency room: three tools to double the rate of diagnosis. J Neurol. 2022 Jan;269(1):294-306. doi: 10.1007/s00415-021-10627-1. Epub 2021 Aug 16. PMID: 34398269.
26. Newman-Toker DE, Curthoys IS, Halmagyi GM. Diagnosing Stroke in Acute Vertigo: The HINTS Family of Eye Movement Tests and the Future of the“"Eye EC”". Semin Neurol. 2015 Oct;35(5):506-21. doi: 10.1055/s-0035-1564298. Epub 2015 Oct 6. PMID: 26444396; PMCID: PMC9122512
27. Kudo Y, Takahashi K, Sugawara E, Nakamizo T, Kuroki M, Higashiyama Y, Tanaka F, Johkura K. Bedside video-oculographic evaluation of eye movements in acute supratentorial stroke patients: A potential biomarker for hemispatial neglect. J Neurol Sci. 2021 Jun 15;425:117442. doi: 10.1016/j.jns.2021.117442. Epub 2021 Apr 9. PMID: 33857735.
28. Mantokoudis G, Korda A, Zee DS, Zamaro E, Sauter TC, Wagner F, Caversaccio MD. Brun'' nystagmus revisited: A sign of stroke in patients with the acute vestibular syndrome. Eur J Neurol. 2021 Sep;28(9):2971-2979. doi: 10.1111/ene.14997. Epub 2021 Jul 16. PMID: 34176187; PMCID: PMC8456911.
29. von Martial R, Leinweber C, Hubert N, Rambold H, Haberl RL, Hubert GJ, Müller-Barna P. Feasibility of Telemedical HINTS (Head Impulse-Nystagmus-Test of Skew) Evaluation in Patients With Acute Dizziness or Vertigo in the Emergency Department of Primary Care Hospitals. Front Neurol. 2022 Feb 11;12:768460. doi: 10.3389/fneur.2021.768460. PMID: 35222226; PMCID: PMC8873087.
30. Morrison M, Kerkeni H, Korda A, Räss S, Caversaccio MD, Abegg M, Schneider E, Mantokoudis G. Automated alternate cover test for‘'HINT'' assessment: a validation study. Eur Arch Otorhinolaryngol. 2022 Jun;279(6):2873-2879. doi: 10.1007/s00405-021-06998-w. Epub 2021 Jul 23. PMID: 34302212; PMCID: PMC9072275.
31. Omary R, Bockisch CJ, De Vere-Tyndall A, Pazahr S, Baráth K, Weber KP. Lesion follows function: video-oculography compared with MRI to diagnose internuclear ophthalmoplegia in patients with multiple sclerosis. J Neurol. 2023 Feb;270(2):917-924. doi: 10.1007/s00415-022-11428-w. Epub 2022 Oct 31. PMID: 36315254; PMCID: PMC9886641.
32. Cohen M, Hesse S, Polet K, Louchart de la Chapelle S, Morisot A, Bresch S, Pesce A, Lebrun-Frenay C. Reliability of mobile video-oculography in multiple sclerosis patients using an iPad: A

prospective validation study. Mult Scler Relat Disord. 2022 Aug;64:103944. doi: 10.1016/j.msard.2022.103944. Epub 2022 Jun 6. PMID: 35679780.

33. Summa S, Schirinzi T, Favetta M, Romano A, Minosse S, Diodato D, Olivieri G, Martinelli D, Sancesario A, Zanni G, Castelli E, Bertini E, Petrarca M, Vasco G. A wearable video-oculography based evaluation of saccades and respective clinical correlates in patients with early onset ataxia. J Neurosci Methods. 2020 May 15;338:108697. Doi
34. Akhand O, Balcer LJ, Galetta SL. Assessment of vision in concussion. Curr Opin Neurol. 2019 Feb;32(1):68-74. doi: 10.1097/WCO.0000000000000654. PMID: 30516648.
35. Thankachan, Biju. (2018). Haptic Feedback to Gaze Events. 10.13140/RG.2.2.28643.50729.
36. Acuña O V, Aqueveque P, Pino EJ. Eye-tracking capabilities of low-cost EOG system. Annu Int Conf IEEE Eng Med Biol Soc. 2014;2014:610-3. doi: 10.1109/EMBC.2014.6943665. PMID: 25570033.
37. Carrie S, Hutton DA, Birchall JPet al. Otitis media with effusion: components which contribute to the viscous properties. Acta Otolaryngol 1992;112:504-11.
38. Cheng JT, Hamade M, Merchant SNet al. Wave motion on the surface of the human tympanic membrane: holographic measurement and modeling analysis. J Acoust Soc Am 2013;133:918-37.
39. Cheng JT, Maftoon N, Guignard Jet al. Tympanic membrane surface motions in forward and reverse middle ear transmissions. J Acoust Soc Am 2019;145:272.
40. Khaleghi M, Cheng JT, Furlong Cet al. In-plane and out-of-plane motions of the human tympanic membrane. J Acoust Soc Am 2016;139:104-17.
41. Wang X, Gan RZ. Surface Motion of Tympanic Membrane in a Chinchilla Model of Acute Otitis Media. J Assoc Res Otolaryngol 2018;19:619-35.
42. Zhang X, Guan X, Nakmali Det al. Experimental and modeling study of human tympanic membrane motion in the presence of middle ear liquid. J Assoc Res Otolaryngol 2014;15:867-81.
43. Jeon D, Cho NH, Park Ket al. In Vivo Vibration Measurement of Middle Ear Structure Using Doppler Optical Coherence Tomography: Preliminary Study. Clin Exp Otorhinolaryngol 2019;12:40-9.
44. Dai C, Wood MW, Gan RZ. Tympanometry and laser Doppler interferometry measurements on otitis media with effusion model in human temporal bones. Otol Neurotol 2007;28:551-8.
45. Dai C, Wood MW, Gan RZ. Combined effect of fluid and pressure on middle ear function. Hear Res 2008;236:22-32.
46. Gan RZ, Dai C, Wood MW. Laser interferometry measurements of middle ear fluid and pressure snegeffects on sound transmission. J Acoust Soc Am 2006;120:3799-810.

47. Ravicz ME, Rosowski JJ, Merchant SN. Mechanisms of hearing loss resulting from middle-ear fluid. Hear Res 2004;195:103-30.
48. Garcia D. Robust smoothing of gridded data in one and higher dimensions with missing values. Comput Stat Data Anal 2010;54:1167-78.
49. Pauly M, Gross M, Kobbelt LP. Efficient simplification of point-sampled surfaces IEEE Visualization. Boston, MA, USA: IEEE, 2002.
50. Limkin EJ, Reuze S, Carre Aet al. The complexity of tumor shape, spiculatedness, correlates with tumor radiomic shape features. Sci Rep 2019;9:4329.
51. Catrakis HJ, Dimotakis PE. Shape complexity in turbulence. Phys. Rev. Lett. 1998;88:968-71.
52. Valentan B, Brajlih T, Drstvensek Iet al. Basic solutions on shape complexity evaluation of STL data. J. Achiev. Mater. Manuf. Eng. 2008;26:73-80.
53. Catrakis HJ, Aguirre RC, Ruiz-Plancarte Jet al. Shape complexity of whole-field three-dimensional space–time fluid interfaces in turbulence. Phys. Fluids 2002;14:3891-8.

Appendix:

Complete Wire Diagram. The two IR lights are powered with 3.3V and connected to ground. The gyroscope and accelerometer are powered with 5V and have the serial data and serial clock connected to the SDA and SCL ports respectively.